Composite Structures 387 (2026) 120323

Contents lists available at ScienceDirect

Composite Structures

journal homepage: www.elsevier.com/locate/compstruct

Neural network-based structural optimization of tow-steered composite panels accounting for polymorphic uncertainty☆

Marc Fina [a,*], Chiara Bisagni [b]

[a] Institute for Structural Analysis, Karlsruhe Institute of Technology (KIT), Kaiserstr. 12, Karlsruhe, 76131, Germany
[b] Department of Aerospace Science and Technology, Politecnico di Milano (POLIMI), Via La Masa 34, Milano, 20156, Italy

ARTICLE INFO

Keywords:
Buckling
Polymorphic uncertainties
Tow-steered composites
Random imperfections
Monte Carlo simulation
Artificial neural network

ABSTRACT

This paper introduces polymorphic uncertainty modeling in the context of structural optimization for tow-steered composite panels. The approach combines random, interval, and fuzzy variables, into advanced models that simultaneously account for both aleatory (inherent variability) and epistemic (lack of knowledge) uncertainty, allowing for more realistic design. Geometric imperfections are represented using random fields, while uncertainty in the fiber path is modeled with fuzzy functions. To reduce the high computational cost in multi-objective design optimization under polymorphic uncertainty, a hierarchical surrogate modeling strategy based on artificial neural networks (ANNs) is presented. Two interconnected ANNs are constructed: the first predicts the buckling load of random imperfect panels, and the second estimates the stochastic output quantities. Fuzzy cumulative distribution functions and a Pareto front are computed to visualize the results. Structural performance and robustness measures are evaluated for a flat and curved tow-steered panel example within a multi-objective buckling design framework under polymorphic uncertainties. The results are compared with deterministic, aleatory-only, and epistemic-only optimization approaches. It is shown that the optimal stacking sequences are similar when maximizing performance, whereas the optima for robust design depend on the uncertainty characteristics.

1. Introduction

The growing demand for sustainability in civil and aerospace engineering is driving the development of advanced numerical methods, design optimization techniques, and new materials. Tow-steered (TS) composites can make a substantial contribution in this regard. Through spatial variation of the fiber orientations, they can outperform classical composites in terms of strength and stiffness, as demonstrated in several studies [1–6]. An interesting capability of TS composites is the high potential to increase the buckling resistance and reduce the imperfection sensitivity of thin-walled structures, see, e.g., [7–9]. Furthermore, the post-buckling behavior can be optimized by tailoring the fibers. In [10], the authors conclude that the influence of the tow-steered layup on post-buckling sensitivity can be exploited to obtain a stiffer nonlinear post-buckling behavior. How structural effects associated with cutouts can be mitigated is investigated, e.g., in [11]. A promising application of TS laminates is the control of bistable behavior in morphing structures [12].

Automated fiber placement (AFP) for VAT composites was introduced in the 1980s [13]. However, manufacturing processes are a primary source of material and geometric uncertainties in VAT composites. As outlined in [6,14–17], major process-induced defects impacting structural integrity include fiber misalignment, discontinuities, wrinkling, as well as gaps and overlaps. To reduce defects like fiber wrinkling, Kim et al. [18] developed the Continuous Tow Shearing (CTS) method, which shears the tow instead of bending it. An example of modeling a CTS cylinder to explore the design space and quantify the effect of shearing on imperfection sensitivity is provided in [19]. A few studies have addressed uncertainty quantification in TS composites. For example, Wang et al. [20] proposed a reliability-based optimization framework to account for stochastic variations in fiber winding angles. Pagani et al. [21] introduced stochastic field models to capture multi-scale defect uncertainties and assess their impact on fiber and matrix stress responses.

However, classical optimization-based design methodologies typically rely on deterministic models, for which defining model parameters based on incomplete or imprecise data can be challenging. Consequently, current design codes often incorporate substantial safety margins to account for the lack of knowledge. This leads to increased

☆ This article is part of a Special issue entitled: 'Rolfes 65th' published in Composite Structures.

* Corresponding author.
E-mail address: marc.fina@kit.edu (M. Fina).

https://doi.org/10.1016/j.compstruct.2026.120323
Received 31 July 2025; Received in revised form 2 March 2026; Accepted 2 April 2026
Available online 2 April 2026

weight, material consumption and costs. In reality, all data and parameters are subject to different types of uncertainty, such as natural variability (aleatory uncertainty) and the incompleteness or imprecise of data (epistemic uncertainty). These uncertainties in geometric and material parameters have a significant impact on the structural behavior of thin-walled structures and must therefore be considered in multi-objective design approaches. Addressing both aleatory and epistemic uncertainties within a unified framework is a subject of ongoing research. Aleatory uncertainty can be quantified using stochastic methods by modeling parameters as random variables, as is commonly employed in probabilistic buckling analysis, see, e.g., [22–25]. In research it is extensively discussed how epistemic uncertainty can be taken into account. The possibility theory, Bayesian approach and imprecise probability are investigated [26]. In possibility theory, fuzzy sets introduced by Zadeh [27] are used to represent the possibility of event occurrence [28]. In contrast, the Bayesian approach is based on an a priori probability distribution (aleatory uncertainty), which is derived from expert knowledge (epistemic uncertainty). The epistemic uncertainty can be reduced by updating the probability distribution with new data using Bayesian updating. However, epistemic and aleatory uncertainties are inherently mixed in this approach. An alternative framework is the concept of imprecise probabilities [29,30], which allows a separation between epistemic uncertainty (e.g., represented by intervals or fuzzy variables) and aleatory uncertainty (represented by random variables). In [31], it is stated that imprecise probabilities characterize the uncertainty of an event using two measures - a lower and an upper probability. According to [32], this characteristic is emphasized as the main distinction from the Bayesian and traditional probabilistic "dogma of precision". Under the term imprecise probability, the concept of polymorphic uncertainties [33,34] can be classified. The idea of polymorphic uncertainty modeling is the consideration of more than one uncertainty characteristic in one parameter [34]. In this concept, the basic uncertainty models (random, interval, fuzzy variables) are combined to advanced uncertainty models. This enables an explicit distinction between different types of uncertainty in the design process and aims to ensure a more realistic modeling. The application of polymorphic uncertainty modeling has already been demonstrated in different civil engineering disciplines, including, wood construction [35], reinforced concrete bridge design [36], soil modeling [37], footbridge design [38], seismic performance of buildings [39], and 3D concrete printing [40] among many others. In [41,42], polymorphic uncertainty modeling is introduced for buckling. Subsequent studies explore sensitivity analysis [43] and a fuzzy safety design concept is proposed in [44].

In a previous study by the authors [45], the epistemic uncertainty of the fiber path in TS composite panels and cylindrical shells is modeled using fuzzy functions, in addition to the aleatory uncertainty of geometric imperfections using random fields. However, these two types of uncertainty are investigated separately in a buckling design optimization, without applying the polymorphic uncertainty approach. The numerical implementation of optimization with polymorphic uncertainties requires a computationally expensive nested loop algorithm consisting of finite element simulation (e.g., buckling analysis), stochastic analysis (e.g., Monte Carlo simulation), fuzzy interval analysis, and an optimization loop. To reduce the computational costs, surrogate models are employed. In this study, a hierarchical surrogate modeling strategy based on neural networks (ANNs) is presented to enable polymorphic uncertainty modeling for TS composites. The strategy is distinguished using of two interconnected ANNs. The first ANN is to predict the buckling load of geometrically imperfect panels. The imperfections as geometric deviation itself as input parameters would lead to a high-dimensional input space. Therefore, the Karhunen–Loève expansion is employed as a dimensionality reduction technique, as proposed for isotopic and classical composite shells in [46,47]. The second ANN is designed to predict stochastic output quantities, such as the mean value of the buckling load. Both ANNs are then used to perform the fuzzy analysis and the multi-objective design optimization. A flat and a curved TS composite panel are investigated, where the aleatory uncertainty of geometric imperfections is quantified by a random field model, and the epistemic uncertainty of the fiber path is modeled by a fuzzy function. The results are visualized by a Pareto front and corresponding fuzzy cumulative distribution functions (CDFs). So-called information reduction measures [48,49] enable the evaluation of the fuzzy-probability based buckling load in terms of the structural performance and robustness. The optimized laminate configurations considering polymorphic uncertainty are compared against deterministic, aleatory-only, and epistemic-only uncertainty quantification methods.

The paper proposes a paradigm shift from classical optimization approaches that rely on deterministic design variables in aerospace structures. It introduces the concept of polymorphic uncertainty modeling, which simultaneously accounts for both aleatory and epistemic uncertainties. The innovative contributions and key features of the work are summarized as follows:

- Polymorphic uncertainty modeling to address combined aleatory and epistemic uncertainties in tow-steered composites
- Comprehensive uncertainty quantification using random fields and fuzzy functions
- Hierarchical surrogate modeling strategy based on neural networks for predicting the buckling loads of geometrically and materially imperfect tow-steered composite panels
- Structural optimization of tow-steered composite panels considering polymorphic uncertainty

First, an overview of polymorphic uncertainty modeling is provided in Section 2. In Section 3, an uncertainty quantification approach for the investigated panels, using fuzzy functions and random fields, is presented. Furthermore, the optimization problem considering polymorphic uncertainties is formulated. Then, a hierarchical surrogate modeling strategy based on ANNs is proposed in Section 4. For the examples of a flat and a curved TS composite panel, the descriptions of the finite element models, the deterministic buckling analysis, the ANN training, and the multi-objective optimization considering polymorphic uncertainty are presented in Section 5. Finally, Section 6 contains concluding remarks and suggestions for future research.

2. Basics of polymorphic uncertainty modeling

This section presents the fundamentals of polymorphic uncertainty modeling, derived from [50–52]. Polymorphic uncertainty modeling aims to describe aleatory and epistemic uncertainty by combining the basic uncertainty models random, interval, and fuzzy variables, see Fig. 1. This concept is introduced by Graf et al. [33,34]. The main idea of this approach is the consideration of more than one uncertainty characteristic in one parameter [34].

Aleatory uncertainty is represented by random variables, whose probability measure is defined by the distribution function $F(x)$ and the corresponding density function $f(x)$. The notation

$$F(x) = F(x, \lambda_X) \quad \text{and} \quad f(x) = f(x, \lambda_X) \tag{1}$$

indicates that both functions $F(x)$ and $f(x)$ are determined by a set of parameters λ_X, such as the mean or standard deviation. If not enough data is available to define an input parameter, the sole use of a random variable can lead to incorrect assumptions, particularly when the distribution type is unknown. Uncertainty caused by incomplete or imprecise data is known as epistemic uncertainty, which can be modeled using interval and fuzzy variables. A fuzzy variable $\tilde{A}$ is defined as

$$\begin{aligned} &\tilde{A} = \{(x, \mu_A(x)) \mid x \in \mathbb{R}\}, \\ &\mu_A(x) : \mathbb{R} \to [0, 1], \\ &\sup_{x \in \mathbb{R}} [\mu_A(x)] = 1, \end{aligned} \tag{2}$$

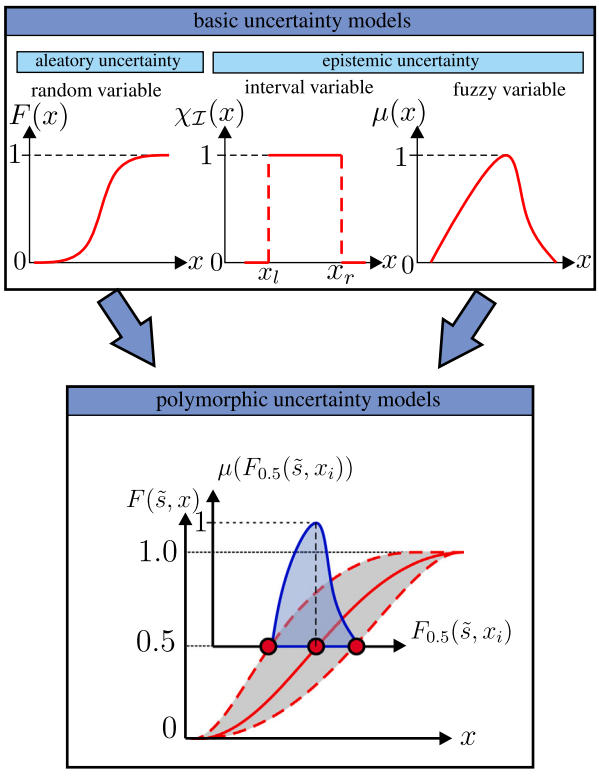

Fig. 1. Polymorphic uncertainty modeling.

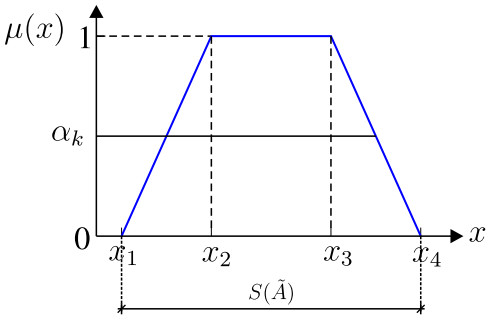

Fig. 2. Trapezoidal fuzzy number.

where $\mu_A(x)$ denotes the membership function, which allows to gradually evaluate the membership of an element x to a set. A specific case occurs when the membership function is constant with $\mu(x) = 1$ for all elements of the set. The resulting crisp set is an interval $[x_l, x_r]$ with $\mu(x_l) = 1$ and $\mu(x_r) = 1$ if $x_l < x_r$. Membership functions can be defined based on linguistic assessments and expert knowledge supported by histogram-based data. For the numerical treatment, the membership function is discretized into α-levels defined by

$$A_{\alpha_k} = \{x \in \mathbb{R} \mid \mu_A(x) \geq \alpha_k\}, \tag{3}$$

which are crisp subsets $[x_{\alpha_{k,l}}, x_{\alpha_{k,r}}]$ (intervals) of the support $S(\tilde{A})$, see Fig. 2.

In this study, for the quantification of epistemic uncertainty convex trapezoidal fuzzy numbers are used as input parameters, expressed as

$$\tilde{A} = \langle x_1, x_2, x_3, x_4 \rangle. \tag{4}$$

Convexity implies that the membership function decreases monotonically on both sides of its peak at $\mu(x) = 1$. However, other shapes of membership functions are also possible, such as triangular forms or functions with nonlinear branches.

The combination of the basic uncertainty models enables the formulation of advanced uncertainty models. For instance, if at least one distribution parameter λ_X (e.g., mean value, standard deviation, etc.) in Eq. (1) is defined as a fuzzy variable, the result is a fuzzy cumulative distribution function (Fuzzy-CDF). The advanced uncertainty model is referred to as a fuzzy probability-based random variable (fp-r) or the fuzzy randomness (fr) model. If at least one distribution parameter is specified as an interval, the result is a probability box (p-box). An alternative term for the model is interval probability-based random variable (ip-r). As shown in Fig. 1, the mean value associated with the CDF value $F(\tilde{s}, x) = 0.5$ is a fuzzy variable. The parameter $\tilde{s}$ is a bunch parameter that contains all predefined fuzzy input variables used for the compact definition of the Fuzzy-CDF.

3. Multi-objective optimization under polymorphic uncertainty

A polymorphic uncertainty quantification approach is proposed for tow-steered composite panels, where geometric imperfections are modeled as random fields and fiber paths are represented by fuzzy functions. Based on this, the multi-objective optimization problem considering polymorphic uncertainty is formulated to quantify structural performance and robustness.

3.1. Polymorphic uncertainty quantification

The spatial variability of geometric imperfections is simulated with random fields. Fundamentals can be derived, e.g., from [52–54]. A random field $\bar{w}(\boldsymbol{x}, \theta)$ assigns random variables to points in space and thus describes aleatory uncertainty that varies over a domain Ω. It can be expressed as

$$\{\bar{w}(\boldsymbol{x}, \theta) \mid \boldsymbol{x} \in \Omega, \theta \in \Theta\}, \quad \boldsymbol{x} = \begin{pmatrix} x \\ y \end{pmatrix}, \tag{5}$$

where θ denotes the possible outcomes in the sample space Θ. A widely used method for generating correlated random fields is the Karhunen–Loève expansion (KLE), which provides dimensionality reduction through a series expansion into orthogonal spatial eigenfunctions weighted by uncorrelated random variables. Spatially correlated random imperfections can be modeled using the series expansion defined as

$$\hat{w}(\boldsymbol{x}, \theta) = \mu + \sigma \sum_{i=1}^{M} \sqrt{\lambda_i}\ \xi_i(\theta)\ \varphi_i(\boldsymbol{x}), \tag{6}$$

where $\xi_i(\theta) \sim \mathcal{N}(0, 1)$ are uncorrelated standard normally distributed random variables, σ denotes the standard deviation and μ the mean value of the field. Since imperfections are defined as geometric deviations from a fixed reference surface, the mean value is set to zero. In the case of panel imperfections, a mean value larger than zero would imply a pure translation of the panel along one spatial direction. Furthermore, $\varphi_i(\boldsymbol{x})$ are the eigenfunctions and λ_i the eigenvalues computed by an eigenvalue problem of the covariance matrix

$$\boldsymbol{C}\,\boldsymbol{\varphi}_i = \lambda_i\,\boldsymbol{\varphi}_i. \tag{7}$$

The entries of the covariance matrix can be computed as

$$C(\boldsymbol{x}_i, \boldsymbol{x}_j) = \rho(\boldsymbol{x}_i, \boldsymbol{x}_j) \quad \text{with} \quad \rho(\boldsymbol{x}_i, \boldsymbol{x}_j) = \rho(d), \tag{8}$$

where the autocorrelation function (acf) $\rho(d) \in [-1, 1]$ depends only on the Euclidean distance d between two points $\boldsymbol{x}_i$, $\boldsymbol{x}_j$, e.g., between two FE nodes:

$$d = |\boldsymbol{x}_j - \boldsymbol{x}_i| = \sqrt{(x_j - x_i)^2 + (y_j - y_i)^2}. \tag{9}$$

The following quadratic exponential acf is chosen to compute the covariance matrix

$$\rho(d) = \exp\left[-\frac{d^2}{\ell_c^2}\right], \tag{10}$$

where, ℓ_c denotes the correlation length. Small lengths lead to uncorrelated fields (wavy shell imperfections), whereas with large correlation lengths strongly correlated fields can be simulated. Finally, the KLE series of M terms in Eq. (6) can be truncated. As described in [24], a reduced number of eigenvalues and eigenfunctions $M < N$ is selected to approximate the random field efficiently. The reduction is performed such that the sum of the eigenvalues is $Q = 99\%$ of the total eigenvalue sum. In this context, Q is defined as a quality index [55] calculated as

$$Q = \frac{1}{\mathrm{tr}(\boldsymbol{C})} \sum_{i=1}^{M} \lambda_i \quad \text{with} \quad \mathrm{tr}(\boldsymbol{C}) = \sum_{i=1}^{N} C_{ii} = \sum_{i=1}^{N} \lambda_i. \tag{11}$$

This possibility of dimension reduction is later used in the paper to significantly reduce the number of input variables for the ANN surrogate model to predict the buckling loads of randomly imperfect panels.

Next, the epistemic uncertainty of the fiber path is described based on the widely used deterministic fiber path definition introduced by [1]

$$\varphi(x') = \phi + (T_1 - T_0)\frac{|x'|}{d} + T_0, \tag{12}$$

where the fiber orientation angle φ of a reference fiber path varies linearly along the coordinate x', from the fiber orientation angle T_0 at a starting point (e.g., the center of the panel) to T_1 at a characteristic distance d (e.g., $d = a/2$ for a square panel with edge length a). The angle ϕ defines the steering direction, along which the tow path varies, while the perpendicular direction is commonly used to define the tow-shift direction. By shifting the reference path perpendicular to the direction of variation (x'-axis), the fiber orientation angle becomes a function of both spatial coordinates: $\varphi = \varphi(x', y')$. To define a stacking sequence for TS composites, the notation $\phi\langle T_0|T_1\rangle$ introduced by [1] is used. However, for the investigated examples, it is always assumed that the local axis x' is not rotated with respect to the global x-axis. Thus, ϕ is neglected, and the notation for the stacking sequence can be reduced to $\pm\langle T_0|T_1\rangle$.

The fiber path defined in Eq. (12) is integrated into the four-node shell element from [56]. The fiber orientation angle is first evaluated at the finite element (FE) nodes and then transformed from the nodes to the four Gaussian points. Within the isoparametric concept, the transformation is expressed as

$$\varphi(\xi, \eta) = \sum_{I=1}^{4} N_I(\xi, \eta)\varphi_I(x, y), \tag{13}$$

where $\varphi_I(x, y)$ denotes the fiber orientation angle evaluated at a specific element node I using Eq. (12), which is interpolated to a desired point (e.g., Gaussian point) in the isoparametric space $\varphi(\xi, \eta)$ using the linear shape functions $N_I(\xi, \eta)$. In [45], a fuzzy fiber path is introduced, formulated as a fuzzy function given by the uncertain mapping

$$\varphi(\boldsymbol{x}', \tilde{\boldsymbol{s}}) : \mathbb{X} \xrightarrow{\sim} \mathcal{F}(\mathbb{Z}) \quad \text{with} \quad \tilde{\boldsymbol{s}} = \begin{pmatrix} \tilde{T}_0 \\ \tilde{T}_1 \end{pmatrix}, \tag{14}$$

where the set of all fuzzy set of the fundamental set $\mathbb{Z} \subseteq \mathbb{R}$ is denoted by $\mathcal{F}(\mathbb{Z})$. Both fiber orientation angles $\tilde{T}_0$ and $\tilde{T}_1$ are modeled as fuzzy variables contained in the fuzzy bunch parameter $\tilde{\boldsymbol{s}}$. Further theoretical foundations to define fuzzy functions can be derived, e.g., from [51]. The fuzzy fiber path with the fiber orientation angles defined by fuzzy trapezoidal numbers, are depicted in Fig. 3.

Based on a deterministic reference fiber path (red solid line), the fiber paths to the membership ($\mu = 1$) (black solid line) and to ($\mu = 0$) (red dashed lines) are defined. It can be observed that a fuzzy variable is assigned to each location. Consequently, due to the differentiation of the fiber path, the fiber orientation angle also becomes a fuzzy variable at every point.

In [57], it is stated that the maximum angle error near the inflection points is approximately 5° and usually in the range of ±2°. This statement of expert knowledge cannot be quantified using a random variable, since no data are available to fit a probability distribution.

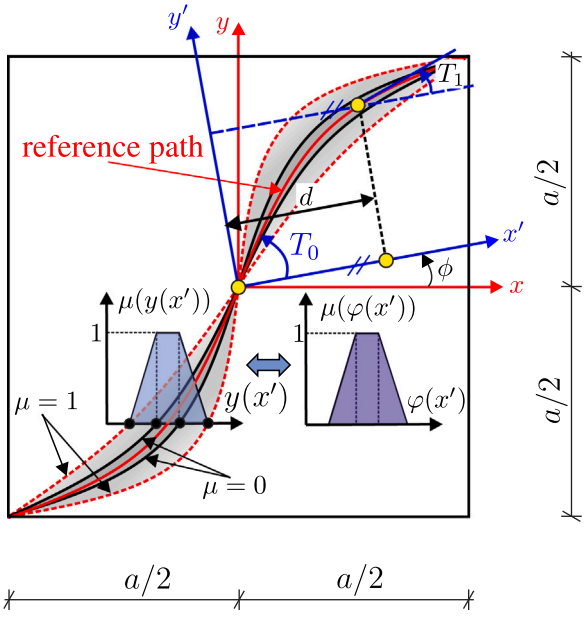

Fig. 3. Fuzzy fiber path and fiber orientations.

However, the epistemic uncertainty of the fiber orientation angles ΔT_0 and ΔT_1 can be quantified, e.g., using two fuzzy trapezoidal numbers defined as

$$\Delta\tilde{T}_0 = \Delta\tilde{T}_1 = \langle -5, -2, +2, +5\rangle. \tag{15}$$

Assuming the fiber angle typically varies within ±2°, full membership is assigned to this range. Outside this range, the membership function decreases linearly to zero at ±5°, which represents the maximum variation occurring only near inflection points.

3.2. Formulation of the optimization problem

The theory of design optimization considering polymorphic uncertainty is derived from [48,49]. The polymorphic uncertainty quantification of geometric imperfections and the fiber orientation angles results in the following buckling optimization problem:

$$\max_{\boldsymbol{x}_d \in D} \tilde{P}_{\mathrm{cr}}(\tilde{\boldsymbol{x}}_d, \tilde{\boldsymbol{x}}_a), \tag{16}$$

where the vector of the design parameters $\tilde{\boldsymbol{x}}_d$ (containing the fuzzy fiber orientation angles) and the a priori parameters $\tilde{\boldsymbol{x}}_a$ (containing the fuzzy/interval parameters of the random field) are uncertain. Consequently, the objective function defined by the mapping

$$\tilde{P}_{\mathrm{cr}}(\tilde{\boldsymbol{x}}_d, \boldsymbol{x}_a) \mapsto \tilde{P}_{\mathrm{cr}} \tag{17}$$

is uncertain, see [45]. An optimizer, e.g., particle swarm [58], requires deterministic output quantities to evaluate the fitness. Therefore, the uncertain output quantities must be post-processed into comparable scalar values. For this purpose, the so-called information reduction measurements (IRMs) proposed in [48,49] are used. The IRMs are categorized into representative measures $\mathfrak{M}$ and uncertainty quantifying measures $\mathfrak{U}$. The representative measures $\mathfrak{M}$ are used to evaluate and optimize performance, while the uncertainty quantifying measures $\mathfrak{U}$ assess the robustness of the structure. The used information reduction measures (IRMs) for the panel optimization are depicted in Fig. 4.

The output quantity on each design point is a fuzzy CDF of the buckling load, where the mean value is defined as a Fuzzy mean value $\tilde{\mathbb{E}}[P_{\mathrm{cr}}]$. Robustness and performance are evaluated using the area $\mathfrak{U}_A(\tilde{\mathbb{E}}[P_{\mathrm{cr}}])$ and the centroid $\mathfrak{M}_{x_S}(\tilde{\mathbb{E}}[P_{\mathrm{cr}}])$ of the fuzzy mean value of the buckling load $\tilde{\mathbb{E}}[P_{\mathrm{cr}}]$, respectively. For instance, an area close to zero

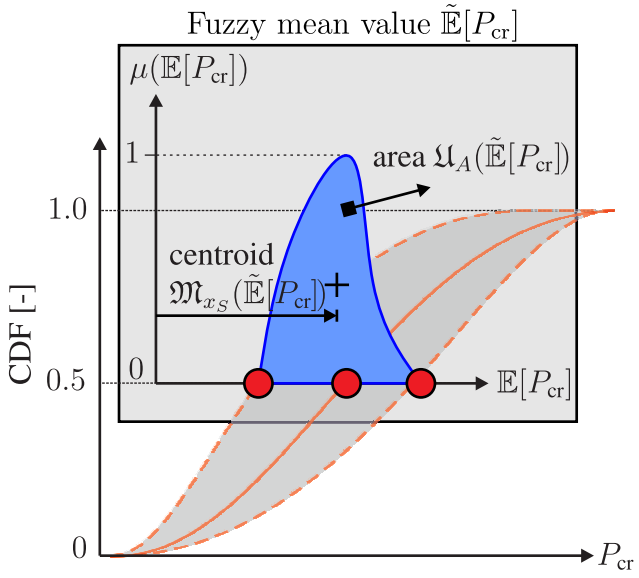

Fig. 4. Representation of the used information reduction measures (IRMs).

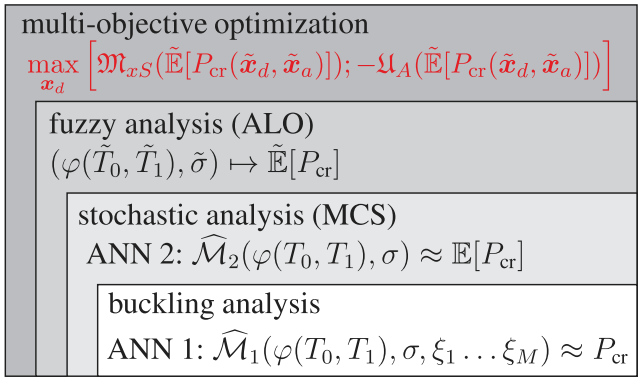

Fig. 5. Multi-loop computational model for structural optimization considering polymorphic uncertainties.

corresponds to a negligible level of uncertainty in the output quantity, while a high value of $\mathfrak{M}_{x_S}$ reflects, on average, larger buckling resistance and thus improved performance. Thus, a multi-objective design optimization problem accounting for polymorphic uncertainties can be formulated as

$$\max_{\boldsymbol{x}_d} \left[\mathfrak{M}_{x_S}(\tilde{\mathbb{E}}[P_{\text{cr}}(\tilde{\boldsymbol{x}}_d, \tilde{\boldsymbol{x}}_a)]); -\mathfrak{U}_A(\tilde{\mathbb{E}}[P_{\text{cr}}(\tilde{\boldsymbol{x}}_d, \tilde{\boldsymbol{x}}_a)])\right], \tag{18}$$

where the negative sign is used to transform the minimization of $\mathfrak{U}_A$, representing increased robustness, into a maximization problem. To illustrate potential conflicts between performance and robustness, the results can be visualized using a Pareto front based on both IRMs.

4. Surrogate model strategy for buckling analysis using ANNs

This section presents the surrogate modeling strategy based on artificial neural networks (ANNs), which enables a multi-objective buckling optimization considering polymorphic uncertainty within a reasonable computational time.

4.1. Multi-loop computational model

A nested multi-loop approach has to be performed as depicted in Fig. 5.

The inner loop contains the FE model for buckling load computations. For the stochastic analysis, the second loop runs a Monte Carlo simulation, repeatedly evaluating the FE buckling analysis to compute the second order statistics, e.g., the mean value of the buckling load $\mathbb{E}[P_{\text{cr}}]$. To reduce the computational effort surrogate models are typically used. Surrogate models to replace the Monte Carlo simulation, e.g., for bounding imprecise failure probabilities of linear structural systems is introduced in [59]. This approach relies on the assumption of a linear mapping between input and output quantities within the used operator norm theory. For buckling analysis, the nonlinear structural behavior must be considered. In [60], the Control Variates method is applied to efficiently estimate the second-order statistics of the buckling loads by leveraging the correlation between the results from the linear and nonlinear buckling analyses. An extended strategy is to construct a first surrogate model to predict the fundamental solution of inner loop, which is then used to construct surrogate models for the other loops (levels), as proposed in [36].

In the present paper, a hierarchical surrogate modeling strategy based on two interconnected neural networks is proposed. The first ANN predicts the buckling load

$$\widehat{\mathcal{M}}_1(\varphi(T_0, T_1), \sigma, \xi_1 \dots \xi_M) \approx P_{\text{cr}} \tag{19}$$

for the fiber orientation angles T_0, T_1, the standard deviation σ of the random imperfection field and standard normally distributed random variables ξ_i from the Karhunen–Loève expansion (KLE) in Eq. (6). This ANN is then used to train a second ANN to predict the mean value of the buckling load

$$\widehat{\mathcal{M}}_2(\varphi(T_0, T_1), \sigma) \approx \mathbb{E}[P_{\text{cr}}]. \tag{20}$$

Both ANNs are depicted in Fig. 6.

A key feature of the first ANN is its capability to predict the buckling loads of structures with geometric imperfections, where the ξ_i's from the Karhunen–Loève expansion (KLE) in Eq. (6) are used as input parameters. This leads to a significant reduction in the number of input parameters compared to directly using the geometric deviation $\hat{w}(\boldsymbol{x}, \theta)$. The concept introduced in [46,47] is further investigated in this study to predict the buckling load of geometrically imperfect TS composite panels.

In summary, the first ANN has to be trained on a relatively large set of up to 15 input variables for the presented examples. The approximated multidimensional response function can be non-monotonic and may exhibit kinks, making an ANN an appropriate choice. However, the second surrogate model (ANN2), which approximates the stochastic output for three input parameters, could potentially be replaced by a simpler surrogate, such as a Lagrange polynomial or a least-squares regression model. In the third loop in Fig. 5, the fuzzy analysis is performed based on the trained ANN to compute the fuzzy mean value of the buckling load $\tilde{\mathbb{E}}[P_{\text{cr}}]$ using the so-called α-level optimization (ALO) [50]. The interval bounds of the fuzzy mean value are calculated on each α-level using the particle swarm optimizer [58] defined as

$$\begin{aligned} \mathbb{E}[P_{\text{cr},\alpha_k,l}] &\approx \min_{s \in \{s_{\alpha_k}\}} \widehat{\mathcal{M}}_2(\boldsymbol{s}) \\ \mathbb{E}[P_{\text{cr},\alpha_k,r}] &\approx \max_{s \in \{s_{\alpha_k}\}} \widehat{\mathcal{M}}_2(\boldsymbol{s}), \end{aligned} \tag{21}$$

where the fuzzy bunch parameters are bounded by the corresponding α-level set

$$\boldsymbol{s} \in [\boldsymbol{s}_{\alpha_k,l}, \boldsymbol{s}_{\alpha_k,r}] = \{\boldsymbol{s}_{\alpha_k}\}. \tag{22}$$

Finally, the centroid and the area of the Fuzzy mean value is calculated and the multi-objective design optimization defined in Eq. (18) is solved with the outer loop.

All uncertainty quantification methods, surrogate models and optimization algorithms are implemented in MATLAB [61]. The surrogate model is based on MATLAB's artificial neural network (ANN) toolbox, modified for buckling design optimization within the multi-loop

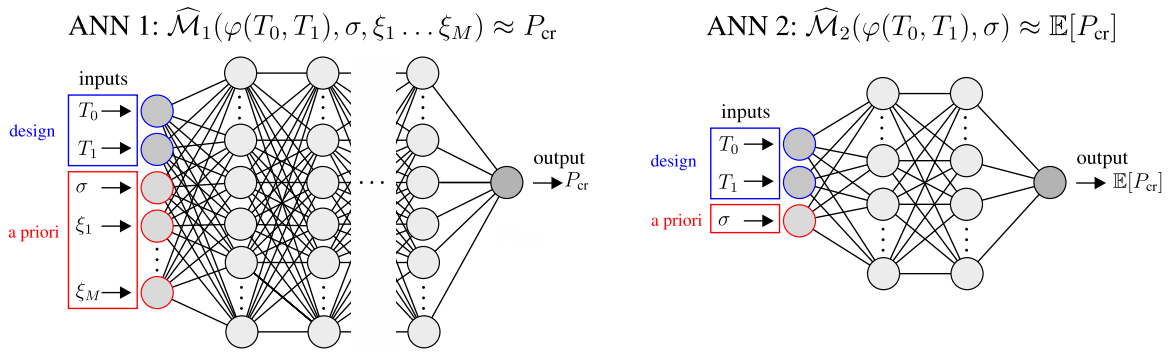

Fig. 6. Architectures of ANN $\widehat{\mathcal{M}}_1$ (left) to approximate the fundamental solution (buckling load P_{cr}) and ANN $\widehat{\mathcal{M}}_2$ (right) to approximate the stochastic solution (e.g., mean of the buckling load $\mathbb{E}[P_{\text{cr}}]$).

framework. The FE buckling analyses are performed using an extended version of the finite element analysis program FEAP [62]. In the developed FEAP–MATLAB interface, all input data associated with each training point are transferred to FEAP, which returns the corresponding results to MATLAB for further evaluation. After successful training, the FEAP routine is replaced by the trained ANN 1. This surrogate model is subsequently used to train the second ANN 2 in MATLAB. A geometrically nonlinear quadrilateral shell element based on [56] is implemented, featuring linear isoparametric shape functions and the assumed natural strain method (ANS) to mitigate shear locking. In the element, the fiber path formulation is incorporated.

4.2. Fundamentals of numerical buckling analysis

Numerical buckling analyses form the inner loop and thus the basis of the computational model for buckling optimization considering uncertainties as depicted in Fig. 5. Therefore, a brief summary of the fundamentals for identifying stability points is provided, before the examples are presented. In general, a non-linear eigenvalue problem is formulated as [60,63,64]:

$$[\boldsymbol{K}_{\text{lin}}+\Lambda\boldsymbol{K}_{\text{nlin}}(\boldsymbol{u})]\,\boldsymbol{\varphi}=\boldsymbol{0}, \tag{23}$$

with the eigenvalue Λ and the corresponding eigenvector $\boldsymbol{\varphi}$. Furthermore, $\boldsymbol{K}_{\text{lin}}$ and $\boldsymbol{K}_{\text{nlin}}$ denote the linear and nonlinear components of the tangent stiffness matrix, respectively, resulting from its decomposition

$$\boldsymbol{K}_T=\boldsymbol{K}_{\text{lin}}+\boldsymbol{K}_{\text{nlin}}=\boldsymbol{K}_{\text{lin}}+\boldsymbol{K}_U(\boldsymbol{u})+\boldsymbol{K}_G(\boldsymbol{\sigma}(\boldsymbol{u})). \tag{24}$$

Depending on the variational formulation, the nonlinear term $\boldsymbol{K}_{\text{nlin}}$ can be decomposed into $\boldsymbol{K}_U$, the initial displacement matrix capturing the influence of pre-buckling deformations, and $\boldsymbol{K}_G$, the geometric stiffness matrix. As further illustrated in Eq. (24), the nonlinear part, and consequently the tangent stiffness matrix, depends on the displacement $\boldsymbol{u}$ and the stress state $\sigma(\boldsymbol{u})$. In Eq. (23), the buckling load can be estimated as

$$\boldsymbol{P}_{\text{cr}}\sim\Lambda\boldsymbol{K}_{\text{nlin}}, \tag{25}$$

where Λ can be interpreted as a load increasing factor. For $\Lambda=1$, Eq. (23) is transformed into the classical eigenvalue problem:

$$(\boldsymbol{K}_{\text{lin}}+\Lambda\boldsymbol{K}_{\text{nlin}})\boldsymbol{\varphi}=\boldsymbol{0}\Leftrightarrow\boldsymbol{K}_T\boldsymbol{\varphi}=\boldsymbol{0}\Leftrightarrow(\boldsymbol{K}_T-\omega\boldsymbol{1})\boldsymbol{\varphi}=\boldsymbol{0}, \tag{26}$$

where the buckling load corresponds to $\omega=0$

In cases where linear pre-buckling behavior is observed, as in the flat panel example, the buckling load $\boldsymbol{P}_{\text{cr}}$ can be computed using a linear buckling analysis (LBA). This analysis starts from the displacement state $\boldsymbol{u}=\boldsymbol{0}$, solving the linear system

$$\boldsymbol{K}_T(\boldsymbol{0})\boldsymbol{u}_0=\boldsymbol{P}_0\quad\Longleftrightarrow\quad\boldsymbol{u}_0=\boldsymbol{K}_T^{-1}(\boldsymbol{0})\boldsymbol{P}_0 \tag{27}$$

for a prescribed external load $\boldsymbol{P}_0$. At this point, the tangent stiffness matrix reduces to the linear stiffness matrix, i.e., $\boldsymbol{K}_T(\boldsymbol{0})=\boldsymbol{K}_{\text{lin}}$. Finally, the linear buckling analysis can be written as

$$[\boldsymbol{K}_{\text{lin}}+\Lambda_0\boldsymbol{K}_{\text{nlin}}(\boldsymbol{u}_0)]\,\boldsymbol{\varphi}_0=\boldsymbol{0}. \tag{28}$$

The corresponding critical load, and displacement state are defined as

$$\tilde{\boldsymbol{P}}_{\text{cr}}=\Lambda_0\boldsymbol{P}_0, \tag{29}$$

$$\tilde{\boldsymbol{u}}_{\text{cr}}=\Lambda_0\boldsymbol{u}_0. \tag{30}$$

The buckling load $\tilde{P}_{\text{cr}}$ can be computed from the associated load vector $\tilde{\boldsymbol{P}}_{\text{cr}}$. In case of non-linear pre-buckling behavior, the results of a linear buckling analysis can significantly differ from the non-linear buckling load. This requires a comprehensive geometrically non-linear path-following analysis using an iterative procedure such as the Newton–Raphson scheme. In the second curved panel example presented in Section 5.2, the nonlinear buckling analysis is carried out using a path-following procedure. Buckling is assessed by monitoring the pivots from the decomposition of the tangent stiffness matrix $\boldsymbol{K}_T=\boldsymbol{L}\boldsymbol{D}\boldsymbol{L}^T$. A change in the sign of these pivots indicates a change in the equilibrium state, according to

$$\begin{array}{llll}\forall D_{ii} & , & D_{ii}>0 & \rightarrow\ \text{stable}\\ \exists D_{ii} & , & D_{ii}=0 & \rightarrow\ \text{indifferent (stability point)}\\ \exists D_{ii} & , & D_{ii}<0 & \rightarrow\ \text{unstable.}\end{array} \tag{31}$$

If at least one diagonal element D_{ii} becomes negative, the computation is terminated and the corresponding load state is saved. At this equilibrium state, the critical load vector $\boldsymbol{P}_{\text{cr}}$ and the initial post-buckling mode $\boldsymbol{\varphi}_{\text{cr}}$ are obtained by solving the nonlinear eigenvalue problem given in Eq. (23). The scalar valued buckling load P_{cr} is subsequently computed from the associated load vector $\boldsymbol{P}_{\text{cr}}$.

5. Numerical examples

The neural network-based structural design optimization considering polymorphic uncertainty is demonstrated on two examples. The first example is a tow-steered flat panel from [1] with a linear pre-buckling behavior. The second example is a tow-steered curved panel, characterized by a strongly nonlinear pre-buckling behavior. In [65], the same panel is studied with a straight fiber laminate. Two neural networks are trained and employed in a multi-objective buckling design optimization framework. From the polymorphic uncertainty quantification of random geometric imperfections and the fuzzy fiber path, as described in Section 3.1, the buckling load is obtained as a fuzzy-probability-based random variable. This allows for evaluation in terms of performance (centroid of the fuzzy mean value of the buckling load $\mathfrak{M}_{x_S}(\mathbb{E}[\tilde{P}_{\text{cr}}])$ and robustness (area of the fuzzy mean value of the buckling load $\mathfrak{U}_A(\mathbb{E}[\tilde{P}_{\text{cr}}])$. Optimal fiber path configurations are analyzed based on the resulting Pareto front. The results are compared to those obtained from deterministic optimization, which does not account for uncertainties, as well as to the findings in [45], where epistemic and aleatory uncertainties are investigated separately.

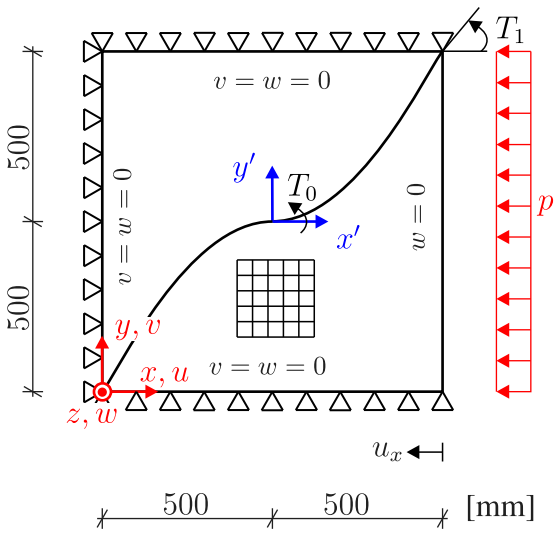

Fig. 7. FE model of the axially loaded tow-steered composite panel with transverse edge restrained boundary conditions.

Table 1
Material properties of the CFRP lamina.

E_{11} [N/mm^2]	E_{22} [N/mm^2]	G_{12} [N/mm^2]	ν_{12} [−−]
180987	10 273	7170	0.28

5.1. Tow-steered flat panel

5.1.1. Deterministic buckling analysis

The finite element (FE) model of the axially loaded panel with a reference fiber path is depicted in Fig. 7.

A square FE mesh of 30 × 30 elements accurately predicts the buckling behavior, as confirmed by a convergence study. Following the study in [1], the panel is investigated under transversely edge restrained (ter) boundary conditions. Along all panel edges the out-of-plane displacements w in the z-direction are fixed, while all rotational degrees of freedom remain free. At the transverse edges ($y = 0$ mm and $y = 1000$ mm), the in-plane displacements v are fixed. The edge at $x = 0$ mm is fixed in the u-direction, while a uniform axial end-shortening u_x is applied along the opposite edge at $x = 1000$ mm. The transversely isotropic material properties of the CFRP laminate are given in Table 1.

The panel consists of a twelve-layer laminate with a symmetric stacking sequence $[\pm\langle T_0|T_1\rangle]_{3s}$. It should be noted that the local coordinate system x', y' to define the fiber path is only shifted and not rotated with respect to the global $x - y$ coordinate system. Consequently, the angle ϕ is set to zero in Eq. (12). Each tow-steered layer has a thickness of $t = 0.127$ mm, yielding a total laminate thickness of $h = 1.524$ mm. Due to the thin-walled design of the panel, buckling occurs before strength failure.

In Fig. 8, samples of random geometric imperfections of the square flat panel with a correlation length of $\ell_c = 750$ mm and different standard deviations $\sigma = 0.5$ mm (left) and $\sigma = 1.5$ mm (right) are depicted.

Since no imperfection measurements are available to assess the correlation properties of the field, a correlation length of $\ell_c = 750$ mm is adopted based on a previous study. In that study, the influence of different correlation lengths on the optimization results is investigated, and identical stacking sequences are obtained for different correlation lengths. As stated in [45], the investigation of other correlation lengths does not provide any additional insights. It should be noted that this is the case for the present example. The influence of the correlation length

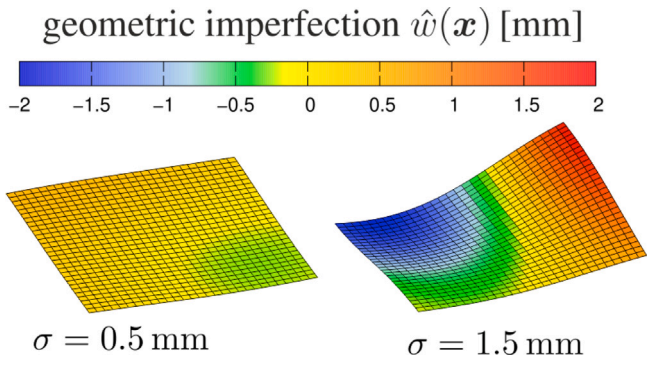

Fig. 8. Samples of random geometric imperfection with $\ell_c = 750$ mm, and different standard deviations $\sigma = 0.5$ mm (left) and $\sigma = 1.5$ mm (right).

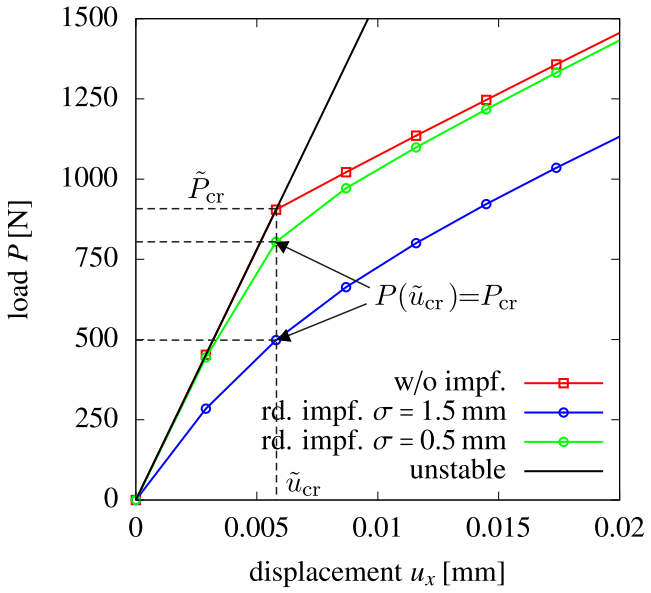

Fig. 9. Load–displacement curves with random imperfections for the flat panel with the stacking sequence of $[\pm\langle 0|50\rangle]_{3s}$.

can be quite large, see, for example, [24,43]. Therefore, the correlation length should be considered as an additional uncertain variable in future works.

Due to the lack of data, a relatively wide interval for the standard deviation of the random imperfection field is chosen in order to additionally quantify the lack of knowledge (epistemic uncertainty): $\bar{\sigma} = [0.5\,\text{mm}, 1.5\,\text{mm}]$. This results in an interval-probability based random field, where on each location of the field a interval probability-based variable (p-box) is assigned, see [52]. If more data become available, a statistical evaluation can be performed and the interval can be narrowed. Alternatively, fuzzy variables can be employed.

First, a deterministic buckling analysis is performed for the panel. Fig. 9 shows the load–displacement curves for the panel configuration $[\pm\langle 0|50\rangle]_{3s}$, with and without applied random imperfections.

The resulting load for an increasing displacement u_x is computed as $P = 1000\,p$, based on the loaded edge length of 1000 mm. The linear buckling analysis of the panel without imperfections yields a buckling load of $\tilde{P}_{\rm cr} = 906$ N and a corresponding critical displacement of $\tilde{u}_{\rm cr} = 0.0058$ mm. The normalized deterministic buckling load

$$\tilde{P}_{\rm cr,norm} = \frac{\tilde{P}_{\rm cr}\, a}{E_{11}\, h^3} \approx 1.414, \tag{32}$$

where a is the edge length in the x-direction, closely matches the normalized deterministic buckling load of 1.44 reported in [1]. A typical

Table 2
Input parameters of the constructed ANNs for the flat panel.

parameter	type	interval
fiber orientation angle T_0 [°]	design	$[-5, 95]$
fiber orientation angle T_1 [°]	design	$[-5, 95]$
std. of the random imperfection field σ [mm]	a priori	[0.5, 1.5]
random variables of the KLE series $\xi_1 \dots \xi_i \dots \xi_{M=7}$ [-]	a priori	$[-3, 3]$

linear pre-buckling behavior can be observed for the panel without imperfections. At the stability point, a small geometric imperfection, e.g., in the form of the first eigenvector $\boldsymbol{\varphi}_1$ scaled by an amplitude of 0.1 mm, is applied to trace the stable post-buckling path (w/o impf., red curve). If no imperfection is applied, the unstable path (solid black line) is followed. For this example of an unstiffened panel, the stability point vanishes if the panel is subjected to imperfections. Therefore, for each laminate configuration, the critical displacement $\tilde{u}_{\text{cr}}$ of the panel without imperfections is calculated by the linear buckling analysis defined in Eq. (28). To predict the critical displacement for arbitrary training and sample points of fiber orientation angles within the input space interval, a least-squares surrogate model is constructed. When the panel is applied with imperfection, it is loaded to the critical displacement and the corresponding load $P(\tilde{u}_{\text{cr}}) = P_{\text{cr}}$ is evaluated as a reference (buckling) load P_{cr}. Note that, in the mathematical sense, this point does not represent a critical load, as the stability point (an indifferent equilibrium state) for the imperfect panel disappears. This can be observed in the green and blue load–displacement curves in Fig. 9, where the panel is subjected to the sample of random geometric imperfections shown in Fig. 8 with standard deviations $\sigma = 0.5$ mm and $\sigma = 1.5$ mm, representing the bounds of the defined input interval. Both curves lie below the red curve (without imperfections). The green curve, corresponding to the smaller standard deviation, deviates only slightly, whereas the blue curve shows a strongly nonlinear behavior, and the load $P(\tilde{u}_{\text{cr}})$ drops significantly.

5.1.2. ANN training

The input parameters of the constructed ANNs are summarized in Table 2.

According to the quality index $Q = 99\%$ defined in Eq. (11), a total of $M = 7$ KLE terms is required. It should be noted that this number depends on the selected correlation length of the random field. The smaller the correlation length, the larger the number M of KLE terms. In this study, a correlation length of $\ell_c = 750$ mm is investigated. The ANN is trained only for this correlation length. If the correlation length is defined, e.g., as a fuzzy (uncertain) parameter, it must be defined as an input variable of the ANN. However, in that case, the eigenvalue problem in Eq. (7) must be solved at every sample point. An efficient implementation of this problem is part of possible future investigations. The bounds for the seven ξ's are defined by a confidence interval of $\pm 3\sigma$ to cover of 99.7% of the standard normal distribution $\mathcal{N}(0, 1)$. Furthermore, the standard deviation of the random field is chosen to $[0.5, 1.5]$ as a further a priori parameter to simulate an interval probability based random field. The input intervals to consider the fuzzy fiber orientation angles is defined to $[-5°, 95°]$. Thus, overlaps within the deterministic design space $T_0, T_1 = [0, 90]$ are considered by the support interval $[-5, 5]$ of the trapezoidal numbers defined in Eq. (15). The first ANN (ANN 1), $\widehat{\mathcal{M}}_1$, is trained using all ten input parameters listed in Table 2 to predict the buckling load P_{cr} of the panel subjected to random imperfections. The training data is generated by numerical buckling analyses using the described FE model.

The second ANN (ANN 2), $\widehat{\mathcal{M}}_2$, is derived from the first and is trained on a reduced input space defined by the fiber orientation angles T_0, T_1, and the standard deviation of the random field σ, in order to predict the expected value of the buckling load, $\mathbb{E}[P_{\text{cr}}]$. For both ANNs,

Table 3
An example of ANN architecture tuning: mean values $\mu_{\text{mse,train}}$, $\mu_{\text{mse,val}}$ $\mu_{\text{mse,test}}$ and standard deviations $\sigma_{\text{mse,train}}$, $\sigma_{\text{mse,val}}$, $\sigma_{\text{mse,test}}$ of the best training, validation, and test MSE values, respectively.

ANN architecture	$\mu_{\text{mse,train}}$	$\mu_{\text{mse,val}}$	$\mu_{\text{mse,test}}$	$\sigma_{\text{mse,train}}$	$\sigma_{\text{mse,val}}$	$\sigma_{\text{mse,test}}$
[20]	502.41	510.50	509.46	90.99	93.22	97.78
[20 20 20]	24.38	25.69	25.91	5.48	4.53	5.87
[20 20 20 20 20]	8.85	10.03	10.03	3.96	4.12	4.29

Table 4
Prediction of the buckling load for the panel without imperfections and the stacking sequence of $[\pm \langle 0|50\rangle]_{3s}$: mean $\mu_{P_{\text{cr}}}$, standard deviation $\sigma_{P_{\text{cr}}}$ and percentage error ϵ between the mean value and the reference buckling load of $P_{\text{cr}} = 906$ N for three different ANN architectures.

ANN architecture	$\mu_{P_{\text{cr}}}$ [N]	$\sigma_{P_{\text{cr}}}$ [N]	ϵ [%]
[20]	904	23.9	0.22
[20 20 20]	954	54.27	5.30
[20 20 20 20 20]	905	80.05	0.11

a fully connected feedforward neural network is constructed using MATLAB. All input values are normalized to the interval $[-1, 1]$, passed through the hidden layers, and transformed back to the physical space of P_{cr} and $\mathbb{E}[P_{\text{cr}}]$ in the output layer. The hyperbolic tangent function is used as the activation function for all neurons in the hidden layers. The networks are trained using the Levenberg–Marquardt backpropagation algorithm with a learning rate of 0.01. The training data for both ANNs is generated using Latin hypercube sampling (LHS) to ensure comprehensive coverage of the input space, which is randomly split into 70% for training, 15% for validation, and 15% for testing. For ANN 1, a total of 10^5 training samples are generated based on the study in [46,47]. The network topologies of both ANNs are determined based on a study in which various configurations with 1 to 5 hidden layers and 5 to 30 neurons per layer are tested. For each topology a batch of 10 ANNs is trained, as illustrated in [66]. The mean values $\mu_{\text{mse,train}}$, $\mu_{\text{mse,val}}$, $\mu_{\text{mse,test}}$ and standard deviations $\sigma_{\text{mse,train}}$, $\sigma_{\text{mse,val}}$, $\sigma_{\text{mse,test}}$ of the best training, validation, and test mean squared errors (MSE) are calculated, and the configuration with the lowest mean MSE is selected. An example of the ANN architecture tuning for three selected architectures for ANN 1 is provided in Table 3.

The ANN with architecture [20 20 20 20 20] (5 hidden layers with 20 neurons each) shows the best training performance. Furthermore, the buckling load for the panel without imperfections and the stacking sequence $[\pm\langle 0|50\rangle]_{3s}$ is predicted. The case "without imperfection" is part of the training space and simulated for $\sigma = 0$ and $\xi_{1-7} = 0$. The mean $\mu_{P_{\text{cr}}}$, the standard deviation $\sigma_{P_{\text{cr}}}$, and percentage error ϵ between the mean value and the reference buckling load of $P_{\text{cr}} = 906$ N are reported in Table 4.

The prediction results for this single sample point apparently indicate similar performance between the ANN with one hidden layer and the ANN with five hidden layers. However, the training performance should not be evaluated based on only one sample value, particularly in the context of uncertainty quantification. Therefore, the cumulative distribution functions (CDFs) for the panel configuration $[\pm\langle 0|50\rangle]_{3s}$ and $\sigma = 1$ mm are calculated, see Fig. 10.

The predicted CDFs obtained from selected ANNs (CDF-ANN 1) of the three architectures are compared with the CDF derived from FE buckling analyses (CDF-FE). The empirical CDFs are calculated using a Monte Carlo simulation (MCS) with 10^4 samples. As shown in Fig. 10, the ANN with one hidden layer cannot accurately predict the entire CDF. In contrast, the CDFs predicted by the ANNs with three and five hidden layers closely match the reference CDF-FE and provide accurate predictions. In particular, the mean value at a CDF level of 0.5, which is especially relevant for the optimization task, is captured with high accuracy. In summary, ANN 1 is capable of reliably predicting

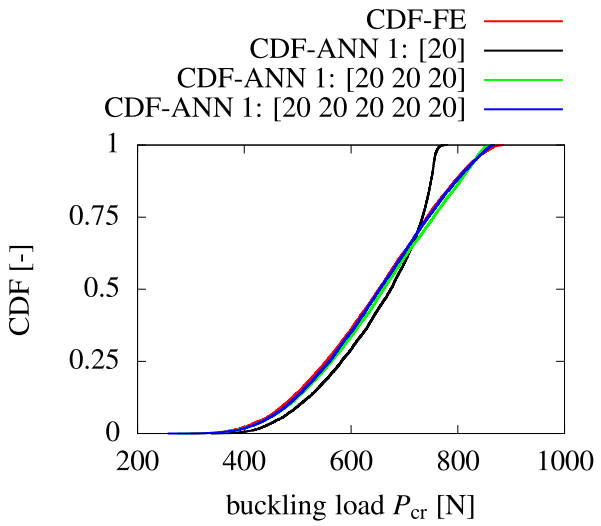

Fig. 10. Cumulative Distribution Functions (CDFs) of the buckling load for the flat panel $[\pm\langle 0|50\rangle]_{3s}$: Finite Element (CDF-FE) vs. artificial neural network (CDF-ANN 1) solution.

the buckling loads of the geometrically imperfect panel. Based on the comparative studies of the different ANN architectures, the network with five hidden layers and 20 neurons per layer is selected.

For the second ANN, $\widehat{\mathcal{M}}_2$, a topology with 2 hidden layers and 20 neurons per layer yields the lowest average MSE. Due to the reduced input space of 3 parameters, a total of 10^4 training samples is sufficient. On each sample point, a MCS with 10^4 realizations is performed using the first ANN with a negligible computational cost. However, in the context of reliability analysis, when very small failure probabilities (10^{-4} to 10^{-6}) must be calculated, a substantially larger number of samples ($> 10^6$) is required. In such cases, the proposed surrogate model can, for example, be combined with LHS to further improve the computational efficiency.

Finally, the loss functions of the MSE via training epochs and correlation plots for both ANNs are depicted in Fig. 11.

In both cases, the mean squared error (MSE) for the training, validation, and test datasets decreases steadily over the training epochs. In particular, the stable MSE on the validation set indicates that the network is well-trained and is not affected by overfitting. This is further confirmed by the correlation plots, which show a strong correlation between the target and predicted values of P_{cr} and the mean value $\mathbb{E}[P_{cr}]$, respectively.

5.1.3. Optimization considering uncertainties

The multilevel surrogate strategy based on the two ANNs enables the solution of the multi-objective design optimization in Eq. (18), accounting for the polymorphic uncertainties described in Section 3.1. Robustness and performance are assessed via the area $\mathfrak{U}_A(\tilde{\mathbb{E}}[P_{cr}])$ and centroid $\mathfrak{M}_{x_S}(\tilde{\mathbb{E}}[P_{cr}])$ of the fuzzy mean value of the buckling load $\tilde{\mathbb{E}}[P_{cr}]$, respectively. The fuzzy mean value is discretized into 10 α-level. At each α-level, the bounds are computed using a particle swarm optimizer, with the second ANN serving as the objective function evaluator. The results of the multi-objective optimization are visualized by a Pareto front with corresponding design points in Fig. 12.

The gray dots represent the feasible solutions evaluated at 361 design points arranged on a regular 19 × 19 grid. A robust panel (buckling response with low inherent uncertainty) is characterized by small values of $\mathfrak{U}_A$, while a high-performance panel is associated with large values of $\mathfrak{M}_{x_S}$. In Fig. 12, it can be observed that the ideal point does not belong to the set of feasible solutions. The Pareto front indicates a conflict, meaning that an increase of the buckling load can only be achieved at the cost of increased uncertainty.

Table 5
Comparison of optimized stacking sequences for the flat panel: deterministic, aleatory-only, epistemic-only and with polymorphic uncertainty quantification (UQ)

UQ method	max performance	max robustness
deterministic	$[\pm\langle 0\|50\rangle]_{3s}$	[–]
aleatory-only	$[\pm\langle 0\|50\rangle]_{3s}$	$[\pm\langle 90\|80\rangle]_{3s}$
epistemic-only	$[\pm\langle 0\|45\rangle]_{3s}$	$[\pm\langle 0\|0\rangle]_{3s}$
polymorphic	$[\pm\langle \mathbf{0}\|\mathbf{55}\rangle]_{\mathbf{3s}}$	$[\pm\langle \mathbf{85}\|\mathbf{90}\rangle]_{\mathbf{3s}}$

Table 6
Values of the area $\mathfrak{U}_A$ and centroid $\mathfrak{M}_{x_S}$ of the fuzzy mean value $\tilde{\mathbb{E}}[P_{cr}]$ from the optimization with polymorphic UQ corresponding to the stacking sequences in Table 5.

stacking sequence	$\mathfrak{U}_A(\tilde{\mathbb{E}}[P_{cr}])$ [N]	$\mathfrak{M}_{x_S}(\tilde{\mathbb{E}}[P_{cr}])$ [N]
$[\pm\langle 0\|50\rangle]_{3s}$	185.57	665.37
$[\pm\langle 0\|45\rangle]_{3s}$	201.38	652.46
$[\pm\langle 0\|55\rangle]_{3s}$	185.08	665.54
$[\pm\langle 90\|80\rangle]_{3s}$	41.35	334.70
$[\pm\langle 0\|0\rangle]_{3s}$	144.53	446.69
$[\pm\langle 85\|90\rangle]_{3s}$	24.88	329.07

Additionally, the Fuzzy mean values of the buckling load $\tilde{\mathbb{E}}[P_{cr}]$, and fuzzy CDFs corresponding to the extreme values $\min \mathfrak{U}_A(\tilde{\mathbb{E}}[P_{cr}])$ and $\max \mathfrak{M}_{x_S}(\tilde{\mathbb{E}}[P_{cr}])$ of the Pareto front are depicted in Fig. 13.

The difference in area between the two fuzzy mean values is clearly illustrated. Centroids of the fuzzy output variables are marked with crosses, and their horizontal positions $\mathfrak{M}_{x_S}$ (performance measure) are also depicted. The fuzzy mean associated with $\max \mathfrak{M}_{x_S}$ has a significantly broader spread, indicating a high degree of uncertainty in the output. In contrast, the fuzzy output associated with $\min \mathfrak{U}_A$ has a very small area, although its centroid is noticeably lower. For instance, an area approaching zero indicates that no uncertainty is present in the output quantity. In Fig. 13 (bottom), the corresponding fuzzy CDFs are shown. These are computed in a post-processing step by dividing the CDF value range from 0 to 1 into 100 discrete intervals. For each CDF value, an interval analysis is performed to determine the bounds of the CDF for $\mu = 0$ and $\mu = 1$ with respect to the three input variables: T_0, T_1 and σ. The interval analysis is based on a HDMR surrogate models, where the bound are calculated using the particle swarm optimizer. The abbreviation HDMR stands for High Dimensional Model Representation, see [67] for the basic principles. HDMR approximates high-dimensional functions by decomposing them into a hierarchy of lower-dimensional component functions, also known as cut-functions. In this study, a second-order HDMR is constructed using a least-squares (LSQ) approximation of the cut-functions with a polynomial degree of 5 and 11 sample points per dimension. This results in a reduced input space of 331 sample points, compared to $11^3 = 1331$ points required for a standard full-factorial LSQ surrogate model with three input parameters. The CDF values for these 331 sample points are then computed using the first ANN, $\widehat{\mathcal{M}}_1$. The bounds of the fuzzy mean values in Fig. 13 (top) can be projected onto the CDF value of 0.5. These are captured with only a small approximation error ϵ resulting from post-processing. Both CDFs appear interval-valued, meaning the left and right bounds for $\mu = 0$ and $\mu = 1$ lie close together, which corresponds approximately to a probability box (p-box). In particular, the wide shape of the CDF linked to $\max \mathfrak{M}_{x_S}$ should be considered in a reliability analysis.

Finally, the results of the optimized stacking sequences for the different uncertainty quantification methods are summarized in Table 5.

In Table 6, the area and centroid values corresponding to the extreme values $\min \mathfrak{U}_A(\tilde{\mathbb{E}}[P_{cr}])$ and $\max \mathfrak{M}_{x_S}(\tilde{\mathbb{E}}[P_{cr}])$ are provided for the stacking sequences listed in Table 5.

The results for the deterministic, aleatory-only, and epistemic-only cases are taken from the previous study [45]. In the aleatory-only

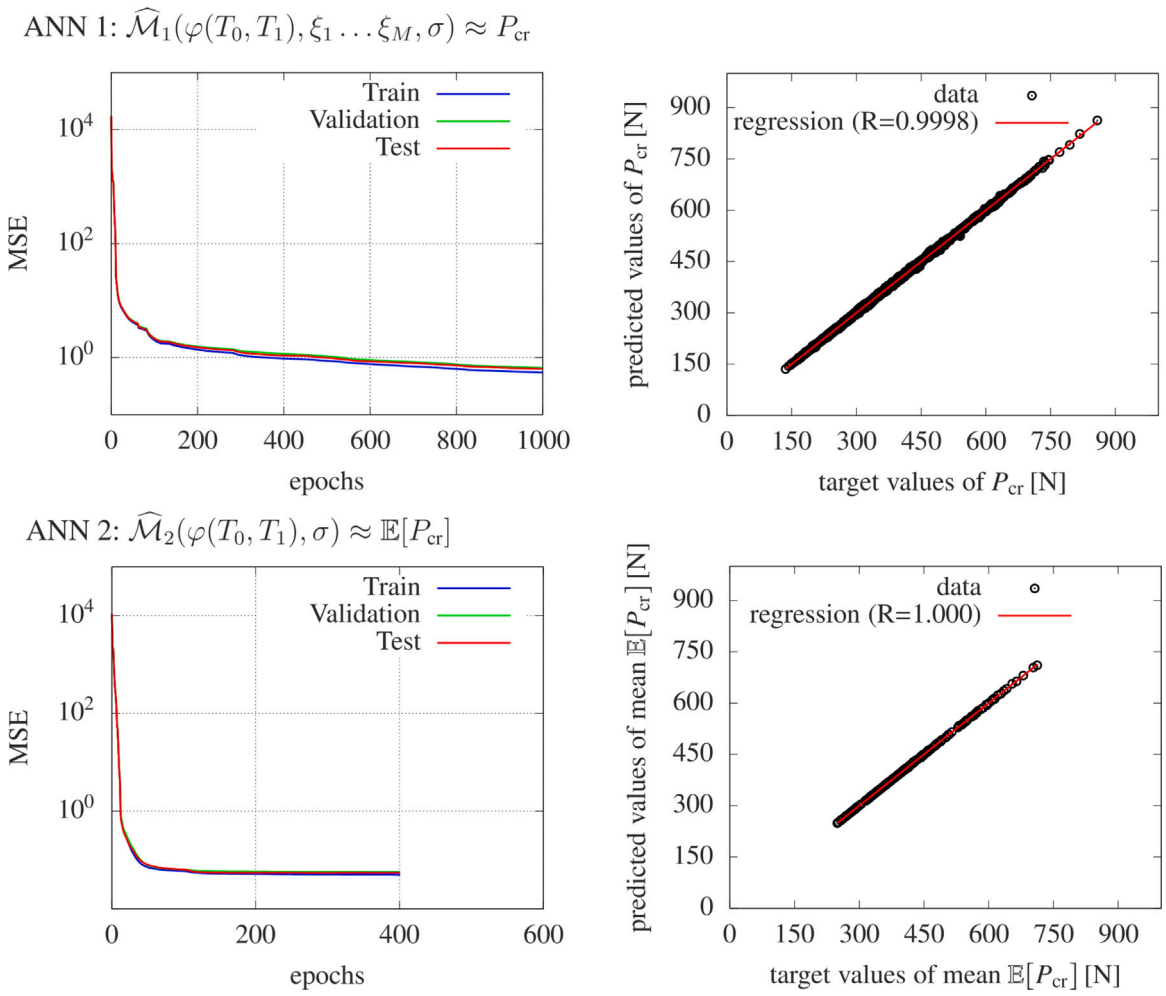

Fig. 11. Loss functions (left) and correlation plots (right) of the trained ANNs for the flat panel.

approach, only the randomness of the geometric imperfections is considered, whereas the fiber paths remain deterministic. In the epistemic-only case, no geometric imperfections are applied, but the fiber paths are defined using fuzzy functions. The optimized stacking sequences obtained using the polymorphic approach, in which both random imperfections and fuzzy fiber paths are modeled, are labeled as "polymorphic". Nearly identical stacking sequences of the tow-steered plies, $[\pm\langle 0|50\rangle]_{3s}$, are obtained across all UQ methods when optimizing for maximum performance ($\max \mathfrak{M}_{x_S}$). This confirms the beneficial effect of tow-steering on structural performance. However, laminates composed entirely of 0° or entirely of 90° plies emerge for maximum robustness ($\min \mathfrak{U}_A$). These laminates have very low buckling loads and consist mostly of straight fibers, exhibit steering angles of at most 10°. Consequently, tow-steering does not appear to reduce the uncertainty of the buckling load, i.e., it does not improve robustness in this example. One possible explanation is that stacking sequences with very low buckling loads, e.g., all 0° and 90° plies, are already close to their minimum performance level and therefore cannot degrade much further. Or in other words, when the buckling load is generally very low, the variation of the buckling load due to random imperfections is also limited. Furthermore, the stacking sequences obtained for the aleatory-only and polymorphic approaches are similar. This can be explained by the strong influence of random imperfections caused by the large range of imperfection amplitudes. Consequently, the aleatory uncertainty dominates the structural response.

5.2. Tow-steered curved panel

5.2.1. Deterministic buckling analysis

A tow-steered curved panel is investigated, see Fig. 14.

The panel has been studied for straight-fiber composite materials, e.g., in [65]. In this work, a tow-steered composite laminate with an eight-ply stacking sequence from [8] is employed: $[\pm 45/\pm\langle T_0|T_1\rangle]_s$. The two outer plies consist of straight fibers, while the inner plies are fiber-steered. The total laminate thickness is $h = 12.7$ mm and the material properties are given in Table 7.

In the center of the panel, the coordinate system x', y' for the fiber path is placed. The coordinate lines are curved in order to define the fiber path on the unfolded surface of 508 × 508 mm. As in the previous example, the angle ϕ that defines the steering direction is set to zero. Consequently, the x', y' system is not rotated with respect to the global Cartesian x, y system. Furthermore, the FE mesh of the panel consists of 30 × 30 elements. Two lateral edges are simply supported with fixed displacements of $u = v = w = 0$, while the remaining edges are free. The panel is subjected to a single load P at the center, where the vertical displacement w_c is measured. In Fig. 15, the load–displacement curves of the curved panel are shown, calculated using the arc-length method with a displacement control of $\Delta w = 0.5$ mm.

A strongly non-linear pre-buckling behavior is observed. In the non-linear buckling analysis, stability points are identified using the criterion defined in Eq. (31). In Fig. 15, the post-buckling path is shown, but is not evaluated in the optimization process, where only

Table 7
Mechanical properties of the composite material.

E_{11} [N/mm^2]	E_{22} [N/mm^2]	G_{12} [N/mm^2]	G_{13} [N/mm^2]	G_{23} [N/mm^2]	ν_{12} [-]
3300	1100	660	660	450	0.3

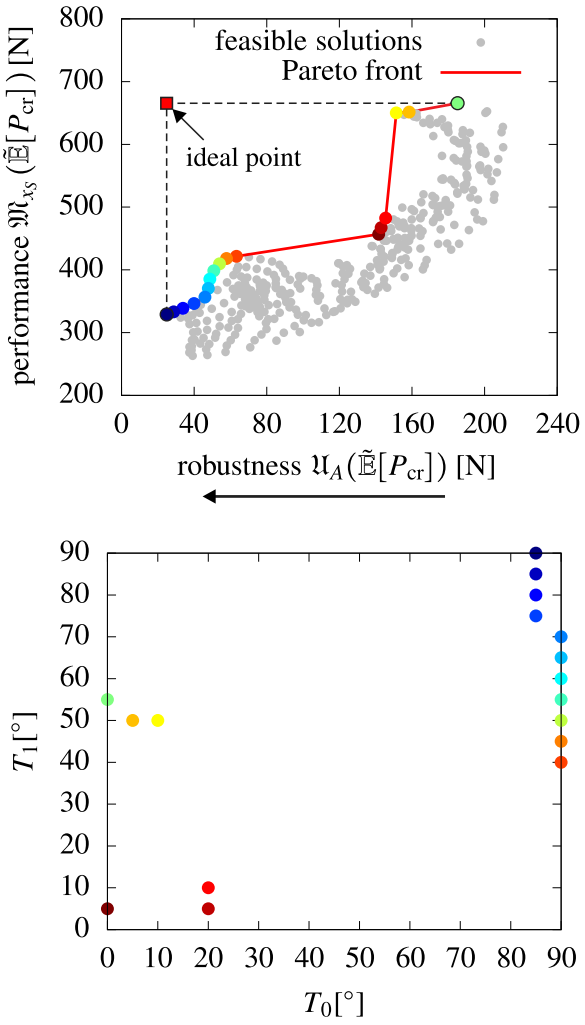

Fig. 12. Results of multi-objective optimization of the flat panel: Pareto front (top) with corresponding design points (bottom)

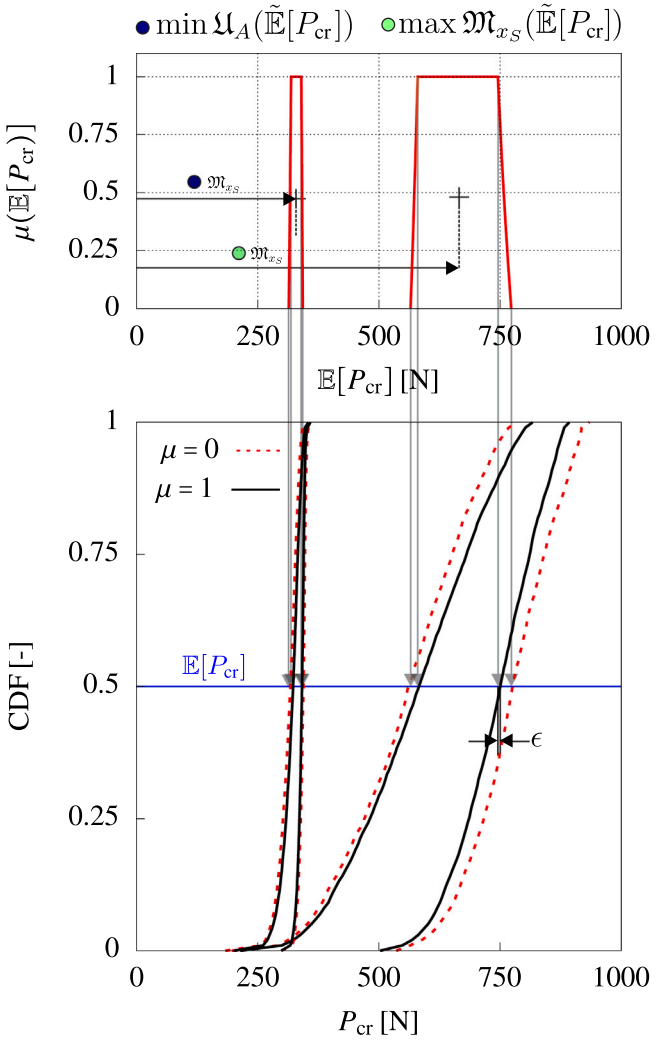

Fig. 13. Fuzzy mean values of the buckling load $\tilde{\mathbb{E}}[P_{cr}]$ (top), and fuzzy CDFs corresponding to the extreme values $\min \mathfrak{U}_A$ and $\max \mathfrak{M}_{x_S}$ of the Pareto front (bottom).

the first buckling point is of interest. In the load–displacement curve shown in Fig. 15, the first pivot becomes negative at the limit point, at which the calculation terminates and the associated load state is stored. However, it should be noted that this shell example can contain bifurcation points before the limit points, see, e.g., [68]. In such cases, the calculation is terminated and the bifurcation point is taken as the buckling point. In a deterministic optimization without random imperfections and uncertain fiber paths, a minimum buckling load of $\min P_{cr} = 1.115$ kN (blue solid curve) and a maximum of $\max P_{cr} = 1.551$ kN (red solid curve) are obtained. The maximum buckling load is associated to stacking sequence of $[\pm 45/\pm\langle 0|0\rangle]_s$. In this case the tow-steered fibers are aligned straight with the principal load-bearing direction, whereas the minimum buckling load results from the stacking sequence $[\pm 45/\pm\langle 90|90\rangle]_s$. This correlates with the results reported in [69], where the panel is investigated for straight fiber laminates. The response function of the deterministic design optimization is depicted in Fig. 16.

Randomly generated imperfections are modeled using the quadratic exponential autocorrelation function in Eq. (10), where the correlation

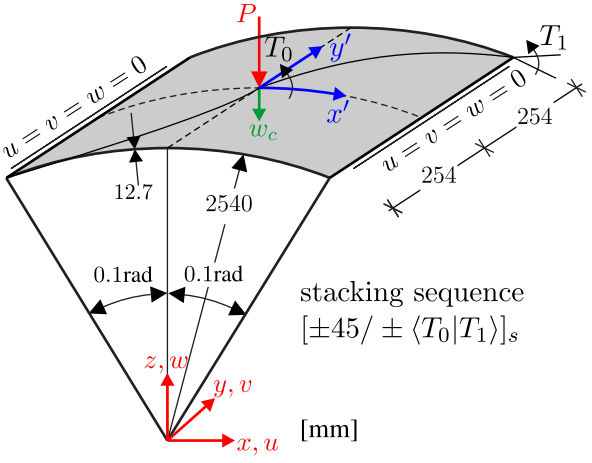

Fig. 14. Model of the tow-steered curved panel.

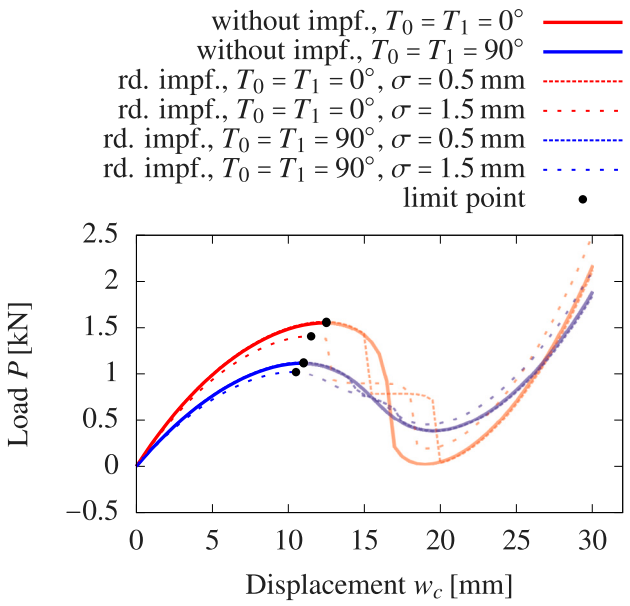

Fig. 15. Load–displacement curves of the curved panel.

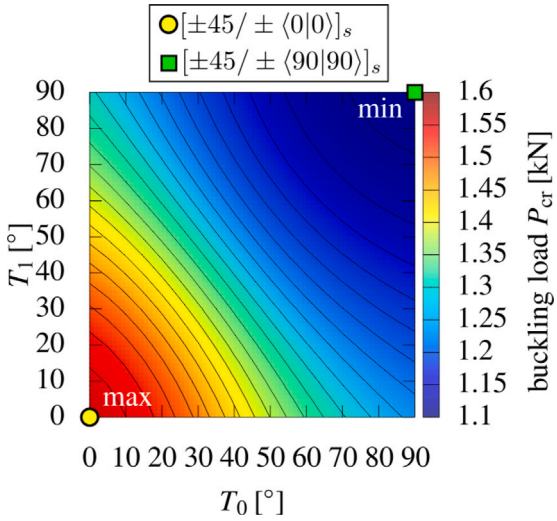

Fig. 16. Deterministic optimization of the flat panel.

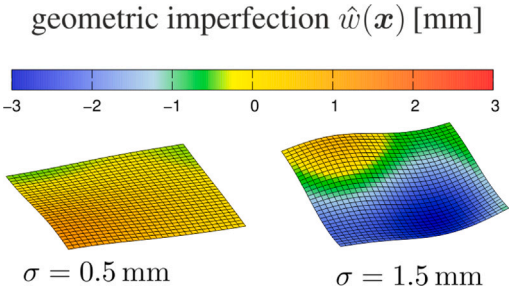

Fig. 17. Samples of random geometric imperfection with $\ell_c = 300$ mm, and different standard deviations $\sigma = 0.5$ mm (left) and $\sigma = 1.5$ mm (right)

length is defined as $\ell_c = 300$ mm. Two samples corresponding to standard deviations of $\sigma = 0.5$ mm and $\sigma = 1.5$ mm, which later define the bounds of the input interval within the polymorphic approach, are shown in Fig. 17.

Table 8
Input parameters of the constructed ANNs for the curved panel.

parameter	type	interval
fiber orientation angle T_0 [°]	design	[−5, 95]
fiber orientation angle T_1 [°]	design	[−5, 95]
std. of the random imperfection field σ [mm]	a priori	[0.5, 1.5]
Young's modulus E_{11} [N/mm^2]	a priori	[2310, 4290]
Young's modulus E_{22} [N/mm^2]	a priori	[770, 1430]
random variables of the KLE series $\xi_1 \cdots \xi_i \cdots \xi_{M=10}$ [-]	a priori	[−3, 3]

These samples are applied to the curved panel. The corresponding load–displacement curves (dotted lines) for the stacking sequences of the minimum and maximum buckling loads are shown in Fig. 15. It can be observed that the imperfections mostly influence the post-buckling behavior, whereas the reduction of the peak load, corresponding to the buckling load, is relatively small.

5.2.2. ANN training

Compared to the previous example of the flat panel in Section 5.1, the input space is increased by five additional variables, see Table 8.

In addition, the Young's modulus in the fiber direction, E_{11}, and transverse to the fiber, E_{22}, are defined as Gaussian random variables, $\mathcal{N}(3300, 330)$ and $\mathcal{N}(1100, 110)$, respectively. The standard deviation σ is set to 10% of the mean value μ and the interval for training the ANN is defined as the ξ's within $\pm 3\sigma$, covering 99.7% of the Gaussian distribution $\mathcal{N}(\mu, \sigma)$. Furthermore, due to the smaller correlation length of $\ell_c = 300$ mm, ten ξ's are needed so that the sum of the eigenvalues accounts for 99% of the total eigenvalue sum in the KLE series defined in Eq. (6). This leads to an increased input space of 15 variables for training the first ANN. The same architectures to those in the previous example are selected: ANN 1 consists of 5 hidden layers with 20 neurons each [20 20 20 20 20], while ANN 2 has 2 hidden layers with 20 neurons each [20 20]. A total of 10^5 training samples for the first ANN is generated using Latin hypercube sampling (LHS), and 10^4 samples for the second ANN with the reduced input space of three variables: T_0, T_1, and σ. The generated samples for training are randomly split into 70% for training, 15% for validation, and 15% for testing. Furthermore, the hyperbolic tangent function is used as the activation function, and the networks are trained using the Levenberg–Marquardt backpropagation algorithm with a learning rate of 0.01. In Fig. 18, the cumulative distribution functions (CDFs) of the buckling load for the curved panel with stacking sequence $[\pm\langle 0|50\rangle]_{3s}$, calculated using the trained ANN (CDF-ANN) and the finite element model (CDF-FE) based on 10^4 samples, are presented.

Both CDFs are quite similar, showing that the trained ANN can accurately predict the buckling load of the imperfect curved panel.

5.2.3. Optimization considering uncertainties

In Fig. 19, the Pareto front of the multi-objective buckling design optimization considering polymorphic uncertainties is depicted.

The feasible solutions (gray dots) are evaluated at 361 design points arranged on a regular 19×19 grid. In contrast to the Pareto front of the previous flat panel in Fig. 12, no pronounced conflict can be observed. Instead, the Pareto front for the curved panel shows a clustering of nearly identical stacking sequences for maximum robustness and a jump to a single optimal stacking sequence for maximum performance. In Table 9, the optimized stacking sequences of the curved panel obtained from the optimization using different uncertainty quantification approaches are summarized.

In addition, Table 10 provides the area and centroid values corresponding to the extreme values $\min \mathfrak{U}_A(\tilde{\mathbb{E}}[P_{cr}])$ and $\max \mathfrak{M}_{x_S}(\tilde{\mathbb{E}}[P_{cr}])$ for the stacking sequences listed in Table 9.

In the aleatory-only approach, only the randomness of the material parameters E_{11}, E_{22} and the geometric imperfection field, for

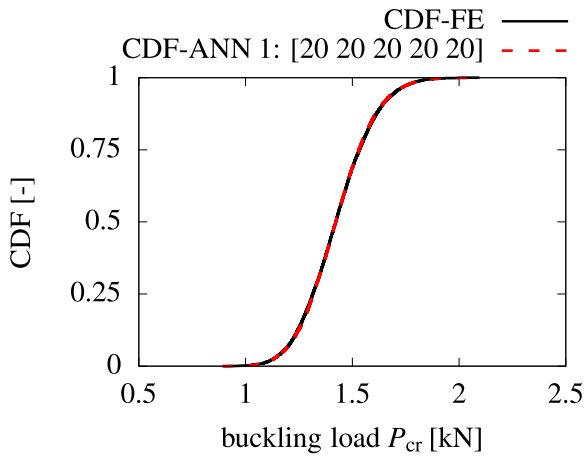

Fig. 18. Cumulative Distribution Functions (CDFs) of the buckling load for the curved panel with the stacking sequence of $[\pm\langle 0|50\rangle]_{3s}$: Finite Element (CDF-FE) vs. Artificial Neural Network (CDF-ANN 1) solution.

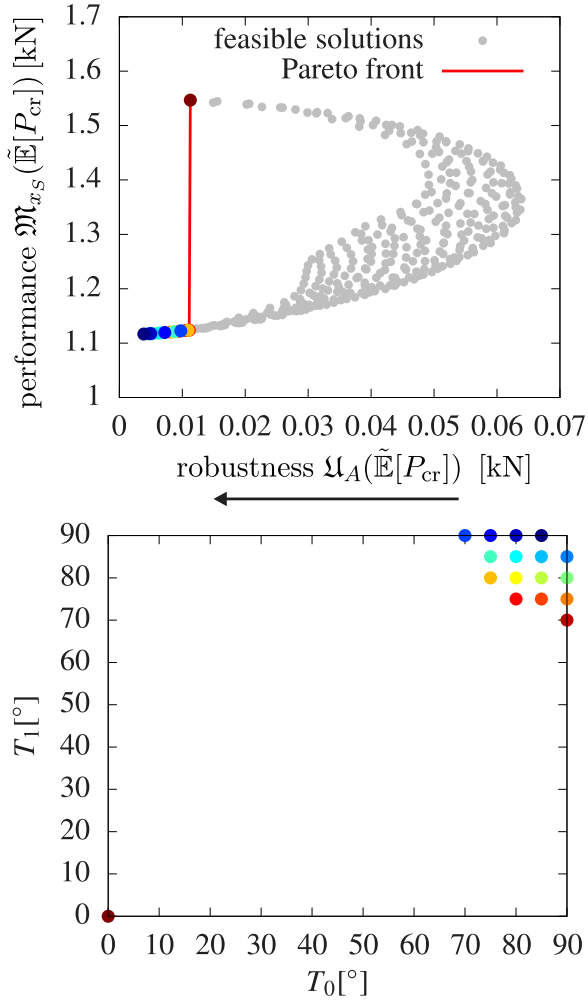

Fig. 19. Results of multi-objective optimization of the curved panel: Pareto front (top) with corresponding design points (bottom).

which the standard deviation is set to $\sigma = 1$ mm, is considered, whereas the fiber orientation angles are treated as deterministic. In the epistemic-only case, no geometric imperfections are applied, but the fiber paths are defined using fuzzy functions. In the polymorphic approach, both random imperfections and fuzzy fiber paths are considered. The resulting stacking sequences are similar across all UQ methods for maximum performance. In these cases, the fiber-steered plies correspond to straight fibers with angles around $T_0 = T_1 = 0°$, such that the fibers are aligned with the principal load-bearing direction. Furthermore, in this example, the stacking sequence obtained from the polymorphic approach is similar to the epistemic-only approach and differs from the aleatory-only approach. However, the robustness measure obtained from the aleatory-only UQ, which is the coefficient of variation (CV), is nearly identical for all stacking sequences. This can be observed in the response function for all UQ methods in Fig. 20 (top right), where the CV is in the range of approximately 10%–13%.

All response functions of the performance optimization show the same shape. Consequently, epistemic uncertainty has a larger influence on robustness in this example.

Table 9
Comparison of optimized stacking sequences for the curved panel: deterministic, aleatory only, epistemic only and polymorphic uncertainty quantification.

UQ method	max performance	max robustness
deterministic	$[\pm\ 45/\pm\ \langle 0\|0\rangle]_s$	[–]
aleatory-only	$[\pm\ 45/\pm\ \langle 5\|0\rangle]_s$	$[\pm\ 45/\pm\ \langle 45\|35\rangle]_s$
epistemic-only	$[\pm\ 45/\pm\ \langle 0\|0\rangle]_s$	$[\pm\ 45/\pm\ \langle 90\|90\rangle]_s$
polymorphic	$[\pm\ 45/\pm\ \langle 0\|0\rangle]_s$	$[\pm\ 45/\pm\ \langle 85\|90\rangle]_s$

Table 10
Values of the area $\mathfrak{U}_A$ and centroid $\mathfrak{M}_{x_S}$ of the fuzzy mean value $\tilde{\mathbb{E}}[P_{cr}]$ from the optimization with polymorphic UQ corresponding to the stacking sequences in Table 9.

stacking sequence	$\mathfrak{U}_A(\tilde{\mathbb{E}}[P_{cr}])$ [kN]	$\mathfrak{M}_{x_S}(\tilde{\mathbb{E}}[P_{cr}])$ [kN]
$[\pm\ 45/\pm\ \langle 0\|0\rangle]_s$	0.0113	1.5468
$[\pm\ 45/\pm\ \langle 5\|0\rangle]_s$	0.0149	1.5423
$[\pm\ 45/\pm\ \langle 45\|35\rangle]_s$	0.0576	1.2924
$[\pm\ 45/\pm\ \langle 90\|90\rangle]_s$	0.0049	1.1172
$[\pm\ 45/\pm\ \langle 85\|90\rangle]_s$	0.0039	1.1167

6. Conclusions

This paper introduces the concept of polymorphic uncertainty modeling in the context of structural optimization for tow-steered composite panels. The epistemic uncertainty of the fiber path is quantified using a fuzzy function, while the geometric imperfections are modeled with random fields. Multi-objective design optimizations under polymorphic uncertainty are computationally expensive. Therefore, a hierarchical surrogate modeling strategy based on artificial neural networks (ANNs) is presented. Two interconnected ANNs are constructed: the first predicts buckling loads of geometrically imperfect panels with high accuracy, and the second ANN is trained using the outputs of the first one to estimate the mean value of the buckling load. Fuzzy CDFs and a Pareto front are computed to visualize the results. To evaluate robustness and performance, the area and centroid of the fuzzy-probability-based buckling load are used as deterministic output quantities to formulate the optimization task. The Pareto front shows that an increase in the performance can only be achieved at the cost of robustness. Furthermore, it is shown that the optimal stacking sequences are similar across all UQ approaches: aleatory-only, epistemic-only, and polymorphic, when maximizing performance. In contrast, the optima for robust design depend on the characteristics of the uncertainties considered in the investigated panel examples. A key message of this paper is therefore to emphasize the importance of simultaneously accounting for both epistemic and aleatory uncertainties using a polymorphic (mixed or hybrid) approach in multi-objective design optimization. By introducing polymorphic uncertainty, the study aims to initiate a paradigm shift away from classical structural optimization approaches

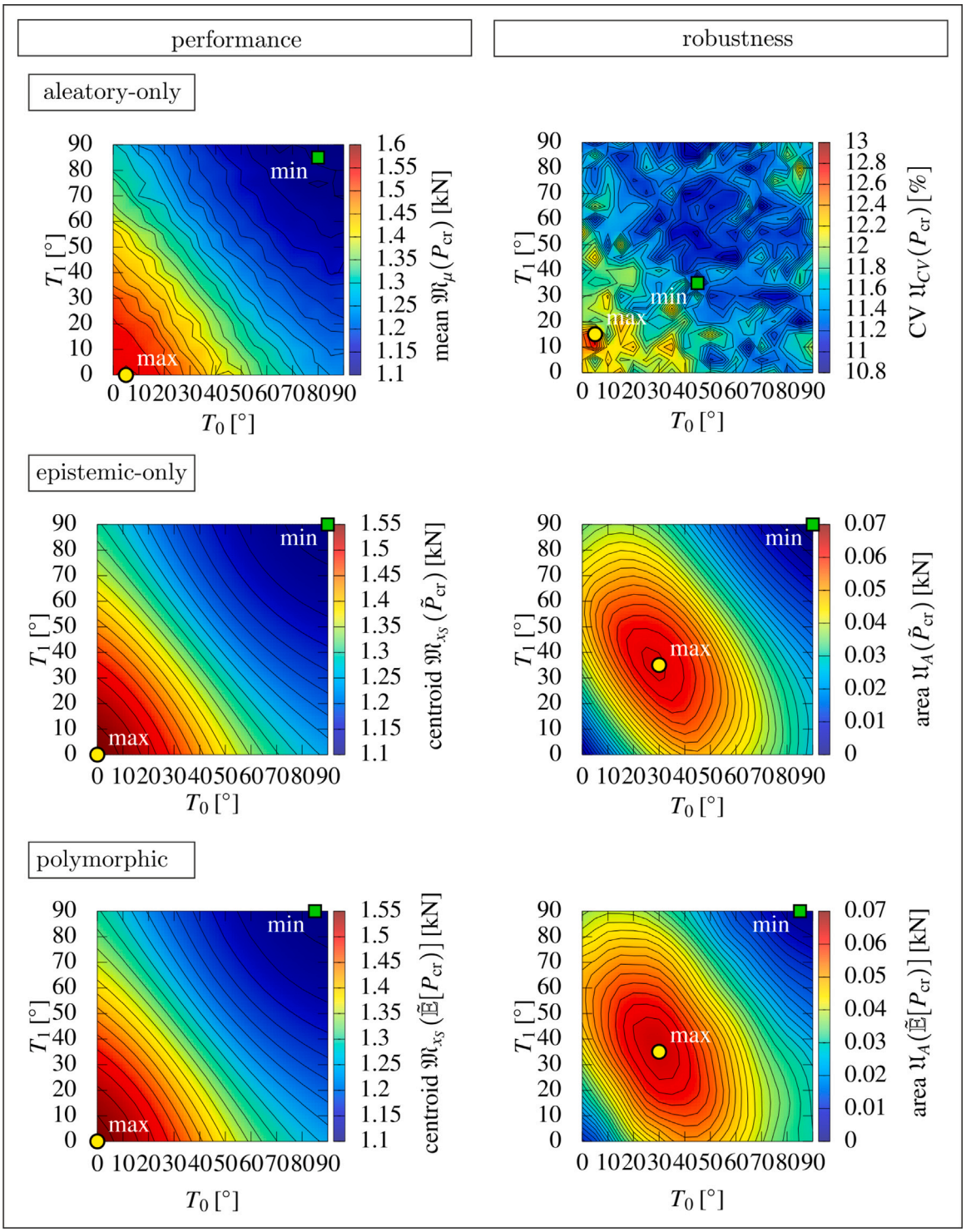

Fig. 20. Response surfaces of the optimization for the different UQ methods: aleatory-only, epistemic-only and polymorphic UQ.

based on deterministic design variables. Alongside the development of new numerical methods, design tools, and materials, it is equally important to advance and integrate uncertainty quantification methods to further improve safety standards and the structural performance.

The proposed approach can be scaled to account for a larger number of uncertain input variables, such as material parameters and parameters to describe boundary and thickness imperfections. The objective is to perform a comprehensive uncertainty quantification based on the available data for each parameter. Future research should focus on extending the proposed methodology to more complex structural systems, including stiffened panels, cylindrical shells, large-scale structures, and morphing adaptive structures, particularly by incorporating manufacturing constraints. However, constructing a robust surrogate model becomes increasingly demanding for complex systems. If the FE model becomes more complex, the random field mesh will likewise increase in complexity, leading to a higher-dimensional input space for the ANN

to predict the buckling load of an imperfect structure. Therefore, to maintain low computational costs, it is essential to develop efficient surrogate modeling techniques, particularly for accurately predicting the stability behavior of imperfect structures.

CRediT authorship contribution statement

Marc Fina: Writing – review & editing, Writing – original draft, Visualization, Validation, Supervision, Software, Resources, Project administration, Methodology, Investigation, Funding acquisition, Formal analysis, Data curation, Conceptualization. **Chiara Bisagni:** Writing – review & editing, Resources, Project administration, Methodology, Funding acquisition.

Declaration of competing interest

The authors declare that they have no known competing financial interests or personal relationships that could have appeared to influence the work reported in this paper.

Acknowledgments

The first author gratefully acknowledges the financial support provided by the Deutsche Forschungsgemeinschaft, Germany (DFG, German Research Foundation) under project number 511267658.

The second author would like to acknowledge the funding by the European Union (ERC Advanced Grant, NABUCCO, project number 101053309). Views and opinions expressed are however those of the authors only and do not necessarily reflect those of the European Union or the European Research Council Executive Agency. Neither the European Union nor the granting authority can be held responsible for them.

References

[1] Gürdal Z, Tatting B, Wu C. Variable stiffness composite panels: Effects of stiffness variation on the in-plane and buckling response. Compos Part A: Appl Sci Manuf 2008;39(5):911–22. http://dx.doi.org/10.1016/j.compositesa.2007.11.015.

[2] Blom A. Structural performance of fiber-placed,variable-stiffness composite conicaland cylindrical shells [Ph.D. thesis], Faculty of Aerospace Engineering, TU Delft; 2010.

[3] Wu K, Stanford B, Turpin J, Martin R. Structural performance of advanced composite tow-steered shells with cutouts. In: 55th AIAA/ASME/ASCE/AHS/ASC structures, structural dynamics, and materials conference. 2014, http://dx.doi.org/10.2514/6.2014-1056.

[4] Brooks T, Martins J, Kennedy G. High-fidelity aerostructural optimization of tow-steered composite wings. J Fluids Struct 2019;88:122–47. http://dx.doi.org/10.1016/j.jfluidstructs.2019.04.005.

[5] Labans E, Bisagni C, Celebi M, Tatting B, Gürdal Z, Blom-Schieber A, Rassaian M, Wanthal S. Bending of composite cylindrical shells with circular cutouts: Experimental validation. J Aircr 2019;56(4):1534–50. http://dx.doi.org/10.2514/1.C035247.

[6] Lopes C. Damage and failure of non-conventional composite laminates [Ph.D. thesis], TU Delft, Faculteit Luchtvaart- en Ruimtevaarttechniek; 2009.

[7] Díaz J, Fagiano C, Abdalla M, Gürdal Z, Hernández S. A study of interlaminar stresses in variable stiffness plates. Compos Struct 2012;94(3):1192–9. http://dx.doi.org/10.1016/j.compstruct.2011.10.016.

[8] Labans E, Bisagni C. Buckling and free vibration study of variable and constant-stiffness cylindrical shells. Compos Struct 2019;210:446–57. http://dx.doi.org/10.1016/j.compstruct.2018.11.061.

[9] Lincoln R, Weaver P, Pirrera A, Groh R. Increasing reliability of axially compressed cylinders through stiffness tailoring and optimization. Philos Trans R Soc A: Math Phys Eng Sci 2023;381(2244):20220034. http://dx.doi.org/10.1098/rsta.2022.0034.

[10] White S, Weaver P, Wu K. Post-buckling analyses of variable-stiffness composite cylinders in axial compression. Compos Struct 2015;123:190–203. http://dx.doi.org/10.1016/j.compstruct.2014.12.013.

[11] Groh R, Wu KC. Nonlinear buckling and postbuckling analysis of tow-steered composite cylinders with cutouts. AIAA J 2022;60(9):5533–46. http://dx.doi.org/10.2514/1.J061755.

[12] Anilkumar P, Haldar A, Clancy G, Scheffler S, Rao B, Weaver P, Rolfes R. Bistable variable stiffness laminates - novel manufacturing and modeling strategies. Mater Des 2025;255:114131. http://dx.doi.org/10.1016/j.matdes.2025.114131.

[13] Lukaszewicz D-J, Ward C, Potter K. The engineering aspects of automated prepreg layup: History, present and future. Compos Part B: Eng 2012;43(3):997–1009. http://dx.doi.org/10.1016/j.compositesb.2011.12.003.

[14] Lozano G, Tiwari A, Turner C, Astwood S. A review on design for manufacture of variable stiffness composite laminates. Proc Inst Mech Eng Part B: J Eng Manuf 2016;230(6):981–92. http://dx.doi.org/10.1177/0954405415600012.

[15] Heinecke F, Willberg C. Manufacturing-induced imperfections in composite parts manufactured via automated fiber placement. J Compos Sci 2019;3(2). http://dx.doi.org/10.3390/jcs3020056.

[16] Ayodele I, Wehbe R, Brasington A, Tatting B, Harik R. Characterization of steered fiber laminates: Perspectives and a survey of the state of the art on principal considerations. Compos Part C: Open Access 2021;4:100118. http://dx.doi.org/10.1016/j.jcomc.2021.100118.

[17] Aragh B, Farahani E, Xu B, G. H, Mansur W. Manufacturable insight into modelling and design considerations in fibre-steered composite laminates: State of the art and perspective. Comput Methods Appl Mech Engrg 2021;379:113752. http://dx.doi.org/10.1016/j.cma.2021.113752.

[18] Kim B, Potter K, Weaver P. Continuous tow shearing for manufacturing variable angle tow composites. Compos Part A: Appl Sci Manuf 2012;43(8):1347–56. http://dx.doi.org/10.1016/j.compositesa.2012.02.024.

[19] Lincoln R, Weaver P, Pirrera A, Groh R. Imperfection-insensitive continuous tow-sheared cylinders. Compos Struct 2021;260:113445. http://dx.doi.org/10.1016/j.compstruct.2020.113445.

[20] Wang Z, Almeida Jr J, St-Pierre L, Wang Z, Castro S. Reliability-based buckling optimization with an accelerated Kriging metamodel for filament-wound variable angle tow composite cylinders. Compos Struct 2020;254:112821. http://dx.doi.org/10.1016/j.compstruct.2020.112821.

[21] Pagani A, Petrolo M, Sánchez-Majano A. Stochastic characterization of multiscale material uncertainties on the fibre-matrix interface stress state of composite variable stiffness plates. Internat J Engrg Sci 2023;183:103787. http://dx.doi.org/10.1016/j.ijengsci.2022.103787.

[22] Kriegesmann B, Rolfes R, Hühne C, Kling A. Fast probabilistic design procedure for axially compressed composite cylinders. Compos Struct 2011;93(12):3140–9. http://dx.doi.org/10.1016/j.compstruct.2011.06.017.

[23] Broggi M, Schuëller G. Efficient modeling of imperfections for buckling analysis of composite cylindrical shells. Eng Struct 2011;33(5):1796–806. http://dx.doi.org/10.1016/j.engstruct.2011.02.019.

[24] Lauterbach S, Fina M, Wagner W. Influence of stochastic geometric imperfections on the load-carrying behaviour of thin-walled structures using constrained random fields. Comput Mech 2018;62(5):1107–25. http://dx.doi.org/10.1007/s00466-018-1554-0.

[25] Wagner H, Hühne C, Elishakoff I. Probabilistic and deterministic lower-bound design benchmarks for cylindrical shells under axial compression. Thin-Walled Struct 2020;146:106451. http://dx.doi.org/10.1016/j.tws.2019.106451.

[26] Götz M. Numerische Entwurfmethoden unter Berücksichtigung polymorpher Unschärfe – Aspekte zeitlicher und räumlicher Abhängigkeiten. 2017, H.32. Institut für Statik und Dynamik der Tragwerke, TU Dresden.

[27] Zadeh L. Fuzzy sets. Inf Control 1965;8(3):338–53.

[28] Dubois D, Prade H. Possibility theory: An approach to computerized processing of uncertainty. New York: Plenum Press; 1988.

[29] Beer M, Ferson S, Kreinovich V. Imprecise probabilities in engineering analyses. Mech Syst Signal Process 2013;37(1):4–29. http://dx.doi.org/10.1016/j.ymssp.2013.01.024.

[30] Faes M, Moens D. Recent trends in the modeling and quantification of non-probabilistic uncertainty. Arch Comput Methods Eng 2020;27(3):633–71. http://dx.doi.org/10.1007/s11831-019-09327-x.

[31] Kozine I, Filimonov Y. Imprecise reliabilities: experiences and advances. Reliab Eng Syst Saf 2000;67(1):75–83. http://dx.doi.org/10.1016/S0951-8320(99)00044-7.

[32] Möller B, Beer M. Engineering computation under uncertainty - Capabilities of non-traditional models. Comput Struct 2008;86(10):1024–41. http://dx.doi.org/10.1016/j.compstruc.2007.05.041.

[33] Graf W, Götz M, Kaliske M. Structural design with polymorphic uncertainty models. In: 6th international conference on reliable engineering computing. 2014.

[34] Graf W, Götz M, Kaliske M. Analysis of dynamical processes under consideration of polymorphic uncertainty. Struct Saf 2015;52:194–201. http://dx.doi.org/10.1016/j.strusafe.2014.09.003.

[35] Schietzold F, Graf W, Kaliske M. Multi-objective optimization of tree trunk axes in glulam beam design considering fuzzy probability based random fields. ASCE-ASME J Risk Uncertain Eng Syst Part B: Mech Eng 2021;7(2). http://dx.doi.org/10.1115/1.4050370.

[36] Freitag S, Edler P, Kremer K, Meschke G. Multilevel surrogate modeling approach for optimization problems with polymorphic uncertain parameters. Internat J Approx Reason 2020;119:81–91. http://dx.doi.org/10.1016/j.ijar.2019.12.015.

[37] Henning C, Ricken T. Polymorphic uncertainty quantification for stability analysis of fluid saturated soil and earth structures. PAMM 2017;17(1):59–62. http://dx.doi.org/10.1002/pamm.201710018.

[38] Schweizer M, Fina M, Wagner W, Kasic S, Freitag S. Uncertain pedestrian load modeling for structural vibration assessment in footbridge design. Eng Struct 2024;311. 118070. http://dx.doi.org/10.1016/j.engstruct.2024.118070.

[39] Weber P, Fina M, Wagner W. Time domain simulation of earthquake excited buildings using a fuzzy stochastic approach. In: Beer M, Zio E, editors. Proceedings of the 29th European safety and reliability conference. 2019, http://dx.doi.org/10.3850/978-981-11-2724-3_0155-cd.
[40] Schmidt A, Lahmer T. Numerical simulation of a 3D concrete printing process under polymorphic uncertainty. In: 9th international workshop on reliable engineering computing. 2021, p. 118–2021.
[41] Fina M, Weber P, Wagner W. Polymorphic uncertainty modeling for the simulation of geometric imperfections in probabilistic design of cylindrical shells. Struct Saf 2020;82. http://dx.doi.org/10.1016/j.strusafe.2019.101894, 101894.
[42] Fina M. Polymorphe Unschärfemodellierung in der nichtlinearen Strukturmechanik – Stabilität von Schalentragwerken, räumliche Variabilität und Metamodellierung [Ph.D. thesis], Institut für Baustatik, Karlsruher Institut für Technologie; 2020, http://dx.doi.org/10.5445/IR/1000129960.
[43] Fina M, Panther L, Weber P, Wagner W. Shell buckling with polymorphic uncertain surface imperfections and sensitivity analysis. ASCE-ASME J Risk Uncertain Eng Syst Part B: Mech Eng 2021;7(2). http://dx.doi.org/10.1115/1.4050165, 020909.
[44] Fina M, Wagner W, Graf W. On polymorphic uncertainty modeling in shell buckling. Computer-Aided Civ Infrastruct Eng 2023;38(18):2632–47. http://dx.doi.org/10.1111/mice.13054.
[45] Fina M, Bisagni C. Buckling design optimization of tow-steered composite panels and cylindrical shells considering aleatory and epistemic uncertainties. Comput Mech 2025;76:59–92. http://dx.doi.org/10.1007/s00466-024-02589-8.
[46] Schweizer M, Fina M, Wagner W, Freitag S. Artificial neural networks for random fields to predict the buckling load of geometrically imperfect structures. Comput Mech 2025;76:181–204. http://dx.doi.org/10.1007/s00466-024-02595-w.
[47] Schweizer M, Fina M, Wagner W, Freitag S. Optimization of shell structures with fuzzy probability-based random fields using artificial neural networks. Proc Appl Math Mech (PAMM) 2025;25(4):e70038. http://dx.doi.org/10.1002/pamm.70038.
[48] Schietzold F, Leichsenring F, Götz M, Graf W, Kaliske M. Robustness versus performance – Nested inherence of objectives in optimization with polymorphic uncertain parameters. Adv Eng Softw 2021;156. http://dx.doi.org/10.1016/j.advengsoft.2020.102932.
[49] Böttcher M, Graf W, Kaliske M. Designing structures with polymorphic uncertainty: Enhanced decision making using information reduction measures to quantify robustness. PAMM 2023;23(4):e202300289. http://dx.doi.org/10.1002/pamm.202300289.
[50] Möller B, Graf W, Beer M. Fuzzy structural analysis using α-level optimization. Comput Mech 2000;26(6):547–65. http://dx.doi.org/10.1007/s004660000204.
[51] Möller B, Beer M. Fuzzy randomness – Uncertainty in civil engineering and computational mechanics. Springer; 2004, http://dx.doi.org/10.1007/978-3-662-07358-2.
[52] Schietzold F, Schmidt A, Dannert M, Fau A, Fleury R, Graf W, Kaliske M, Könke C, Lahmer T, Nackenhorst U. Development of fuzzy probability based random fields for the numerical structural design. GAMM-Mitt 2019;42(1):e201900004. http://dx.doi.org/10.1002/gamm.201900004.
[53] Sudret B, Kiureghian AD. Stochastic finite element methods and reliability – A state-of-the-art report. 2000,
[54] Vanmarcke E. Random fields: Analysis and synthesis. Singapore: World Scientific; 2010.
[55] Baitsch M. Optimierung druckbeanspruchter Stabtragwerke unter Berücksichtigung geometrischer Imperfektionen [Ph.D. thesis], Lehrstuhl für Ingenieurinformatik im Bauwesen, Ruhr-Universität Bochum; 2003.
[56] Wagner W, Gruttmann F. A robust non-linear mixed hybrid quadrilateral shell element. Internat J Numer Methods Engrg 2005;64(5):635–66. http://dx.doi.org/10.1002/nme.1387.
[57] Kim B, Weaver PM, Potter K. Manufacturing characteristics of the continuous tow shearing method for manufacturing of variable angle tow composites. Compos Part A: Appl Sci Manuf 2014;61:141–51. http://dx.doi.org/10.1016/j.compositesa.2014.02.019.
[58] Kennedy J, Russell E. Particle swarm optimization. In: Proceedings of ICNN'95 - international conference on neural networks. 1995, p. 1942–8. http://dx.doi.org/10.1109/ICNN.1995.488968.
[59] Fina M, Lauff C, Faes MGR, Valdebenito MA, Wagner W, Freitag S. Bounding imprecise failure probabilities in structural mechanics based on maximum standard deviation. Struct Saf 2023;101. http://dx.doi.org/10.1016/j.strusafe.2022.102293, 102293.
[60] Fina M, Valdebenito MA, Wagner W, Broggi M, Freitag S, Faes MGR, Beer M. Control variates method to estimate stochastic buckling loads. Internat J Numer Methods Engrg 2025;126(13):e70070. http://dx.doi.org/10.1002/nme.70070.
[61] Mathworks. Matlab. R2023b. 2023, http://www.mathworks.com.
[62] Taylor RL. Finite element analysis program (FEAP). 2025, http://www.ce.berkeley.edu/projects/feap/.
[63] Wagner W, Wriggers P. A simple method for the calculation of postcritical branches. Eng Comput 1988;5(2):103–9. http://dx.doi.org/10.1108/eb023727.
[64] Wagner W. A note on FEM buckling analysis. Commun Numer Methods Eng 1995;11(2):149–58. http://dx.doi.org/10.1002/cnm.1640110208.
[65] Wagner W, Gruttmann F. A simple finite rotation formulation for composite shell elements. Eng Comput 1994;11(2):145–76. http://dx.doi.org/10.1108/02644409410799209.
[66] Gottardi N, Freitag S, Meschke G. Real-time estimation of the structural utilization level of segmental tunnel lining. Undergr Space 2024;17:132–45. http://dx.doi.org/10.1016/j.undsp.2023.11.011.
[67] Rabitz H, Aliş ÖF. General foundations of high-dimensional model representations. J Math Chem 1999;25(2):197–233. http://dx.doi.org/10.1023/A:1019188517934.
[68] Groh R, Pirrera A. Orthotropy as a driver for complex stability phenomena in cylindrical shell structures. Composite Struct 2018;198:63–72. http://dx.doi.org/10.1016/j.compstruct.2018.05.013.
[69] Gruttmann F, Wagner W. A coupled two-scale shell model with applications to layered structures. Internat J Numer Methods Engrg 2013;94(13):1233–54. http://dx.doi.org/10.1002/nme.4496.